



Gas Dynamics in the Galaxy: Total Mass Distribution and the Bar Pattern Speed

Zhi Li^{1,2}, Juntao Shen^{2,3,5}, Ortwin Gerhard⁴, and Jonathan P. Clarke⁴¹ Tsung-Dao Lee Institute, Shanghai Jiao Tong University, Shanghai 200240, People's Republic of China; zli0804@sjtu.edu.cn² Department of Astronomy, School of Physics and Astronomy, Shanghai Jiao Tong University, 800 Dongchuan Road, Shanghai 200240, People's Republic of China
jtshen@sjtu.edu.cn³ Key Laboratory for Particle Astrophysics and Cosmology (MOE)/Shanghai Key Laboratory for Particle Physics and Cosmology, Shanghai 200240, People's Republic of China⁴ Max-Planck-Institut für Extraterrestrische Physik, Gießenbachstraße, D-85748 Garching, Germany

Received 2021 March 19; revised 2021 October 11; accepted 2021 November 8; published 2022 January 26

Abstract

Gas morphology and kinematics in the Milky Way contain key information for understanding the formation and evolution of our Galaxy. We present hydrodynamical simulations based on realistic barred Milky Way potentials constrained by recent observations. Our model can reproduce most features in the observed longitude–velocity diagram, including the Central Molecular Zone, the Near and Far 3 kpc arms, the Molecular Ring, and the spiral arm tangents. It can also explain the noncircular motions of masers from the recent BeSSeL2 survey. The central gas kinematics are consistent with a mass of $6.9 \times 10^8 M_\odot$ in the Nuclear Stellar Disk. Our model predicts the formation of an elliptical gaseous ring surrounding the bar, which is composed of the 3 kpc arms, the Norma arm, and the bar-spiral interfaces. This ring is similar to those “inner” rings in some Milky Way analogs with a boxy/peanut-shaped bulge (e.g., NGC 4565 and NGC 5746). The kinematics of gas near the solar neighborhood are governed by the Local arm. The bar pattern speed constrained by our gas model is $37.5\text{--}40 \text{ km s}^{-1} \text{ kpc}^{-1}$, corresponding to a corotation radius of $R_{\text{CR}} = 6.0\text{--}6.4 \text{ kpc}$. The rotation curve of our model rises gently within the central $\sim 5 \text{ kpc}$, significantly less steep than those predicted by some recent zoom-in cosmological simulations.

Unified Astronomy Thesaurus concepts: [Milky Way Galaxy \(1054\)](#); [Barred spiral galaxies \(136\)](#); [Interstellar medium \(847\)](#); [Milky Way dynamics \(1051\)](#); [Astrophysical fluid dynamics \(101\)](#)

1. Introduction

The observed strong noncircular motions of atomic and molecular gas in the central region of the Galaxy (Burton & Liszt 1978; Bally et al. 1987; Dame et al. 2001) revealed the presence of a stellar bar decades ago (Liszt & Burton 1980; Gerhard & Vietri 1986; Binney et al. 1991). Many features in the observed (l, v) diagram, which shows the distribution of gas emission line intensity or brightness temperature as a function of Galactic longitude l and line-of-sight (LOS) velocity v , can be explained by the periodic orbits in a barred potential. This is because the gas streamlines away from shock regions following the periodic orbits with small deviations (e.g., Roberts et al. 1979; Englmaier & Gerhard 1997; Regan & Teuben 2004; Kim et al. 2012; Sormani et al. 2015a, 2015b). Thus the (l, v) diagram offers tight constraints on the Galactic potential, especially in the central part. Besides the (l, v) diagram, the Bar and Spiral Structure Legacy (BeSSeL) survey (Brunthaler et al. 2011) obtained the position and 3D velocity of nearly two hundred high-mass star-forming regions (HMSFRs) with high-precision Very Long Baseline Interferometry (VLBI) data (e.g., Reid et al. 2019). The peculiar motions of HMSFRs are found to be large ($\sim 50 \text{ km s}^{-1}$) around the bar end, which is likely related to the bar and large-scale spiral arm dynamics.

There have been many attempts to model the global gas features in the Milky Way (MW; e.g., Englmaier & Gerhard 1999;

Fux 1999; Bissantz et al. 2003; Rodriguez-Fernandez & Combes 2008; Baba et al. 2010; Pettitt et al. 2014, 2015; Sormani et al. 2015c; Li et al. 2016), but no models have yet explained all of the observed (l, v) features and the motion of HMSFRs simultaneously. The reason is probably due to the complexity of the Galactic structures. The Galactic bar exhibits a boxy/peanut (b/p) geometry in the central $\sim 2 \text{ kpc}$ (Dwek et al. 1995; Wegg & Gerhard 2013; Ness & Lang 2016; Simion et al. 2017), then it gradually transitions into a long thin bar extending to $l \approx 27\text{--}30^\circ$ (Hammersley et al. 2000; Benjamin et al. 2005; Cabrera-Lavers et al. 2008; Wegg et al. 2015). The overall shape is similar to the buckled bars that are vertically thick in the inner region as seen in N -body simulations (Combes & Sanders 1981; Raha et al. 1991; Martinez-Valpuesta et al. 2006; Shen et al. 2010; Li & Shen 2015). The b/p geometry generates a weaker quadrupole in the potential compared to a pure triaxial ellipsoid with the same surface density, thus it may need to be taken into account in dynamical models (e.g., Fragkoudi et al. 2016).

Besides the bar, the effects of the large-scale spiral arms are also important for modeling gas flows (e.g., Bissantz et al. 2003; Pettitt et al. 2014; Seo & Kim 2014). The nearby five spiral arms, namely the Outer, Perseus, Local, Sagittarius, and Scutum Arms, have been extensively studied with different tracers in recent years (see the reviews by Xu et al. 2018 and Shen & Zheng 2020). The observed arms have pitch angles in a range of $10^\circ\text{--}20^\circ$, and some of them may extend up to $\sim 15 \text{ kpc}$ from the Galactic Center (GC; Dame & Thaddeus 2011). While the shape of the spiral pattern is relatively well constrained, a compelling dynamical explanation for the origin of this spiral pattern in our Galaxy is still lacking (but see the discussion in Sellwood et al. 2019), and different spiral driving mechanisms may have distinct effects on stars and gas.

⁵ Corresponding author.



Stellar dynamical models developed in recent years have significantly improved our understanding of the gravitational potential of the MW (see the reviews by Bland-Hawthorn & Gerhard 2016). For example, the made-to-measure (m2m) models in Portail et al. (2017; hereafter P17) reproduced well the observed star counts and stellar kinematics in the bulge and bar region, and many parameters of the bar (e.g., mass, pattern speed, length, axis ratio, orientation with respect to the Sun, etc.) are relatively well constrained. Similarly, from a sample of ~ 200 maser sources with proper motions and parallaxes, the morphology of the Milky Way’s spiral arms and the kinematics for the star-forming disk are also well constrained (Reid et al. 2019). In addition, rotation curve measurements outside the bar radius have achieved an unprecedented precision with the help of the Gaia data (e.g., Eilers et al. 2019). These constraints on the Milky Way’s potential already provide a valuable starting point for the investigation of the gas flow in the present paper.

Our goal in this paper is to construct a gas dynamical model that can explain the observed gas kinematics (i.e., the (l, v) diagram and the HMSFRs), such that we can use it to further constrain the bar pattern speed and the overall potential of the Milky Way inside the solar circle. To combine with the stellar results, we adopt the m2m potentials in P17 as inputs. We would like to see: (1) how well the m2m models agree with gas kinematics, and (2) whether we can use gas kinematics to provide independent and additional constraints on the bar pattern speed, Ω_b , as well as the mass distribution of the Galaxy. We aim to provide a better gravitational potential model for the MW by combining the stellar and gas dynamics, which would be useful for many other studies.

The paper is organized as follows: we describe our Galactic potential models in Section 2 and constraints from observations in Section 3. The numerical methods are discussed in Section 4. We present the constrained gas models in Section 5, the pattern speed measurements from gas dynamics in Section 6, and the related mass distributions in different regions in Section 7. We discuss the implications of this work and compare our results with those of other studies in Section 8, and summarize in Section 9.

2. Galactic Gravitational Potential

We follow a similar approach to constrain the Galactic potential Φ_{gal} as in our earlier work (Li et al. 2016). The potential Φ_{gal} adopted in this work is a superposition of several components that dominate in different regions Equation (1). More specifically, we include a potential Φ_{ns} of the nuclear structures, a potential Φ_{sp} of two pairs of two arm spirals in the outer disk, a potential Φ_{bs} of the bar-spiral transition interface, and a potential Φ_{pl} to shift the rotation curve in a radial range of 3–7.5 kpc. All of these components are superimposed on a basis potential Φ_{m2m} from the P17 m2m models.

$$\Phi_{\text{gal}} = \Phi_{\text{m2m}} + \Phi_{\text{ns}} + \Phi_{\text{sp}} + \Phi_{\text{bs}} + \Phi_{\text{pl}} \quad (1)$$

We then evolve a gas disk under such a potential and use the gas properties in the MW as observational constraints. We adjust the parameters of the above components until the combined potential Φ_{gal} can generate a gas disk that reproduces most observed features. The mass of the main components in our potentials are summarized in Table 1.

In Figure 1 we show the rotation curves and the corresponding resonances based on two Φ_{gal} used in our models that can best reproduce the observations. One model

Table 1
Masses of Different Components in our Model

Component	Mass (M_{\odot})	Reference
Nuclear Stellar Cluster	0.61×10^8	Chatzopoulos et al. (2015)
Nuclear Stellar Disk	6.90×10^8	Sormani et al. (2020a)
Boxy-peanut bulge	1.34×10^{10}	Portail et al. (2017)
Long thin bar	0.54×10^{10}	Portail et al. (2017)
Bar-spiral interface	0.44×10^8	Section 2.4
Four arm spiral	8.39×10^8	Section 2.3

has a bar pattern speed of $\Omega_b = 37.5 \text{ km s}^{-1} \text{ kpc}^{-1}$, and the other has $\Omega_b = 40 \text{ km s}^{-1} \text{ kpc}^{-1}$. We define these two models as the fiducial models in this work. The shaded regions indicate the differences of the rotation curves between these two, and the blue line is the averaged rotation curve. From the observational side, the pink dots are from Sofue et al. (2009) based on terminal velocities of the interstellar medium (ISM). Note the high velocity peak at $R < 2 \text{ kpc}$ indicated by the pink dots may not reflect the real mass distribution due to the presence of large noncircular motions of gas in this region (Binney et al. 1991; Chemin et al. 2015). The blue stars are from Eilers et al. (2019) based on Jeans modeling of red giants, and the orange dotted–dashed line is from McGaugh (2019), who further included the spiral arms in the Jeans modeling to refine the rotation curve. The purple triangles and the green dotted–dashed lines are from Reid et al. (2019) based on the kinematics of HMSFRs and young stars. The lines and points seem to relatively agree with each other at $R \gtrsim 5 \text{ kpc}$, but there are still uncertainties inside this radius where the bar dominates the potential. In the right panel we show the corresponding frequency curves and the resonances of the fiducial models. For the model with $\Omega_b = 37.5 \text{ km s}^{-1} \text{ kpc}^{-1}$, the corotation radius (CR) is 6.4 kpc, the inner Lindblad resonance (ILR) is 1.0 kpc, the outer Lindblad resonance (OLR) is 10.8 kpc, the inner 4:1 resonance is 3.1 kpc, and the outer 4:1 resonance is 8.7 kpc. For $\Omega_b = 40 \text{ km s}^{-1} \text{ kpc}^{-1}$ these values are 6.0, 0.9, 10.1, 2.9, and 8.2 kpc, respectively. For the spiral arms with the pattern speed of $\Omega_{\text{sp}} = 23 \text{ km s}^{-1} \text{ kpc}^{-1}$, the CR is 10.4 kpc, the ILR is 2.2 kpc, and the inner 4:1 resonance is 6.8 kpc. Note in our model the bar OLR and the spiral CR are quite close to each other.

Figure 2 shows the non-axisymmetric properties of the potential in the fiducial model with $\Omega_b = 37.5 \text{ km s}^{-1} \text{ kpc}^{-1}$. The left and middle panels illustrate the radial and tangential force (F_R and F_{φ}) distributions at the midplane ($z = 0$). The shape of the bar and spirals, as well as their dominated regions, is clearly seen in the plots. The right panel shows the multipoles of the potential obtained from Fourier decomposition. The bar leads to significant Φ_2 and Φ_4 components inside $R \sim 5 \text{ kpc}$, while the spiral contributes to the wiggles of Φ_4 and Φ_6 at larger radius. Multipoles with orders higher than Φ_8 are not important in our potentials.

In the following subsections, we explain in detail how we model the different potential components. Note the values of the parameters in Sections 2.2 and 2.5 are from the fiducial models that are discussed in the main part of this paper.

2.1. Bulge-bar-disk Potential from Made-to-measure Modeling

The basis potentials used in this work are from the best-fit m2m models in P17. The m2m models were constructed from a set of N -body barred disks that were adiabatically adapted to

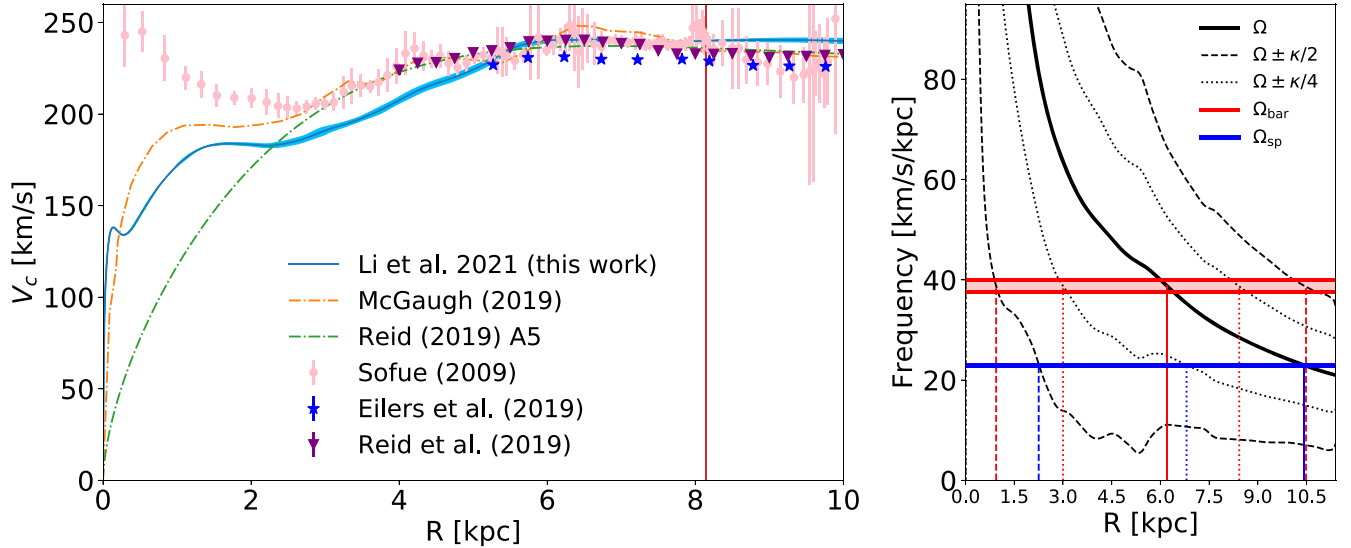


Figure 1. Left panel: the circular rotation curve of the Milky Way based our fiducial gas models with $\Omega_b = 37.5 \text{ km s}^{-1} \text{ kpc}^{-1}$ and $\Omega_b = 40 \text{ km s}^{-1} \text{ kpc}^{-1}$, and the comparison with other studies. The rotation curves in the models are obtained by azimuthally averaging Φ_{gal} . The shaded light blue region shows the differences of the rotation curves between the model with the two bar pattern speeds. The blue line plots the middle values in the shaded region. The vertical red line indicates the adopted solar radius $R_{\odot} = 8.15 \text{ kpc}$ as in Reid et al. (2019). Right panel: corresponding frequency curves and resonances in our fiducial model. The solid black line $\Omega(R)$ is obtained based on the blue line in the left panel, and other black lines are calculated according to the solid black line. The two horizontal red lines indicate the two bar pattern speeds, and the vertical red lines represent the mean resonance radii of the two bar pattern speeds. The blue lines are those for the spiral pattern.

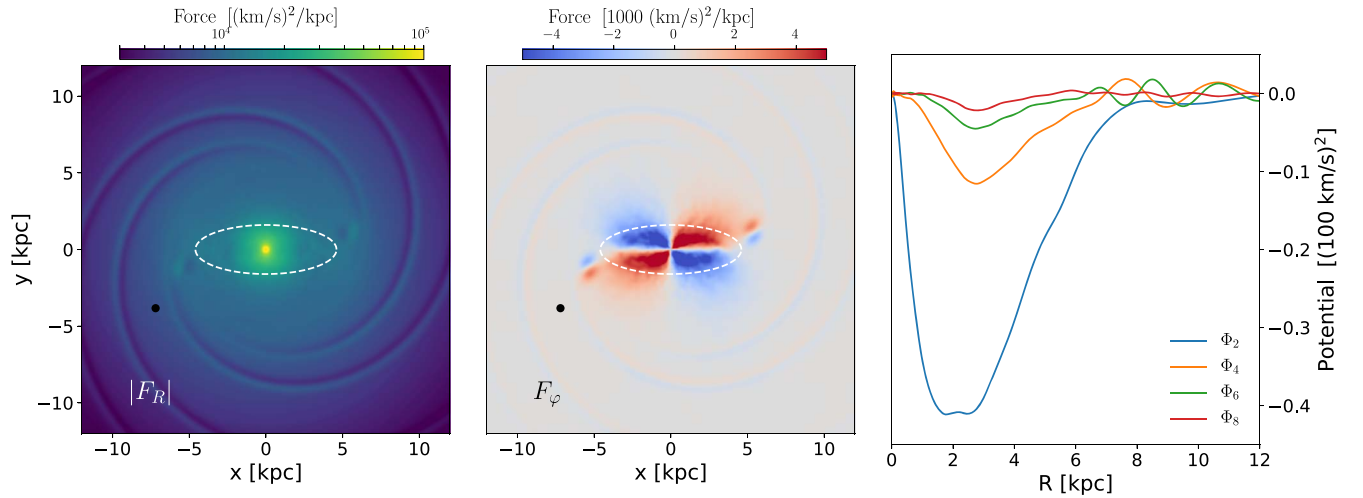


Figure 2. Non-axisymmetric properties of the potential in the fiducial model with $\Omega_b = 37.5 \text{ km s}^{-1} \text{ kpc}^{-1}$. Left panel: the map of the radial force F_R at the midplane ($z = 0$). The white dashed ellipse roughly outlines the size and shape of the bar. The black dot indicates the adopted location of the Sun. Middle panel: the map of the tangential force F_{φ} at the midplane ($z = 0$) generated by the bar and spirals. The kinks around the bar ends show the bar-spiral interface described by Equation (8). Right panel: the quadrupole Φ_2 , octupole Φ_4 , and higher-order multipoles (Φ_6 and Φ_8) of the potential as a function of radius.

match the following observed quantities. The density profiles of the m2m models are constrained by the red clump giants (RCGs) in the bulge and bar region from VVV, 2MASS, and UKIDSS; the kinematics are constrained with data from the BRAVA, OGLE, and ARGOS surveys. For detailed information about the m2m models we refer the readers to P17.

We consider four gravitational potentials from the m2m models in P17, all adjusted to the bulge/bar data assuming the same mass-to-clump ratio and Nuclear Stellar Disk (NSD) mass, but with different bar pattern speeds of $\Omega_b = 35.0, 37.5, 40.0,$ and $42.5 \text{ km s}^{-1} \text{ kpc}^{-1}$, placing the bar corotation radius at $R_{\text{CR}} = 6.72, 6.25, 5.83,$ and 5.42 kpc from the GC, respectively. The mass distributions of these four models are also slightly different, resulting in different rotation curves. We average Φ_{m2m} in the m2m models over a short time period to

remove local fluctuations. We further impose an up-down symmetry of the potential with respect to the Galactic midplane ($z = 0$).

2.2. Nuclear Components

The nuclear component used in P17 is an elongated exponential disk following the bar orientation with an axis ratio of 2:1. However, our gas model prefers an axisymmetric central mass distribution as the gas is observed to have nearly circular motions at $R \sim 100 \text{ pc}$ (e.g., Henshaw et al. 2016). We therefore replace this elongated disk with the fiducial model (model 3) in Sormani et al. (2020a), who used Jeans modeling to constrain the central mass distribution. This central mass model is axisymmetric and is composed of two components: the Nuclear Stellar Cluster (NSC) and the NSD. The NSC is a

compact stellar nucleus that dominates the potential of the MW at $1 \text{ pc} \lesssim R \lesssim 30 \text{ pc}$, while the NSD is a flattened stellar structure that governs the potential at $30 \text{ pc} \lesssim R \lesssim 300 \text{ pc}$ (e.g., Launhardt et al. 2002; Chatzopoulos et al. 2015; Gallego-Cano et al. 2020; Sormani et al. 2020a). Their density profiles are described by the following equations:

$$\rho_{\text{NSC}}(R, z) = \frac{(3 - \gamma)M_{\text{NSC}}}{4\pi q} \frac{a_0}{a^\gamma(a + a_0)^{4-\gamma}}, \quad (2)$$

$$\rho_{\text{NSD}}(R, z) = \rho_1 \exp\left[-\left(\frac{a}{R_1}\right)^{n_1}\right] + \rho_2 \exp\left[-\left(\frac{a}{R_2}\right)^{n_2}\right]. \quad (3)$$

The central density used is the sum of these two components with an additional scaling factor α :

$$\rho_c(R, z) = \rho_{\text{NSC}} + \alpha\rho_{\text{NSD}}. \quad (4)$$

In the above equations, a is defined as $a(R, z) \equiv \sqrt{R^2 + z^2/q^2}$. The NSC density profile is from Equation (17) of Chatzopoulos et al. (2015), with parameters $\gamma=0.71$, $q=0.73$, $a_0=5.9 \text{ pc}$, and $M_{\text{NSC}}=6.1 \times 10^7 M_\odot$. The NSD density profile is obtained by deprojecting Model 2 of Gallego-Cano et al. (2020), with parameters $q=0.37$, $n_1=0.72$, $n_2=0.79$, $R_1=5.06 \text{ pc}$, $R_2=24.6 \text{ pc}$, $\rho_1/\rho_2=1.311$, $\rho_2=1700 M_\odot \text{ pc}^{-3}$, and the scaling factor $\alpha=0.9$ (see also Equations (27)–(30) in Sormani et al. 2020a). This configuration gives a total central (NSC + NSD) mass of $7.5 \times 10^8 M_\odot$, with an enclosed mass at $R=100 \text{ pc}$ of $4.5 \times 10^8 M_\odot$. The corresponding gravitational potential Φ_{ns} is numerically calculated based on Equation (4).

2.3. Spiral Arms

The spiral arms are modeled with the same equations used in Li et al. (2016), which are modified from those in Junqueira et al. (2013). These equations describe the potential of a four armed spiral pattern following (Georgelin & Georgelin 1976; Russeil 2003; Hou & Han 2014; Reid et al. 2014, 2019):

$$\Phi_{\text{sp}}(R, \varphi, z) = \begin{cases} -\zeta_{\text{sp}} R \exp\{-R/\epsilon_{\text{sp}} - |kz|\} \\ -\frac{R^2}{\sigma_w^2} [1 - \cos(m\varphi - f_m)] \} & R \geq R_{\text{sp}} \\ -\zeta_{\text{sp}} R \exp\{-R/\epsilon_{\text{sp}} - |kz|\} \\ -\frac{R^2}{\sigma_w^2} [1 - \cos(m\varphi - f_m)] \} \\ \times \exp[-(R - R_{\text{sp}})^2/2\sigma_{\text{sp}}^2] & R < R_{\text{sp}}, \end{cases} \quad (5)$$

with the shape function f_m and wavenumber k :

$$f_m(R) = m \left(\frac{\ln(R/R_n)}{\tan i} + \gamma \right), \quad (6)$$

and

$$k = m/(R \tan i). \quad (7)$$

The parameters are set to be: the amplitude $\zeta_{\text{sp}}=800.0 \text{ km}^2 \text{ s}^{-2} \text{ kpc}^{-1}$, the half-width of the spiral arms $\sigma_w=2.35 \text{ kpc}$, the scale length of the spiral $\epsilon_{\text{sp}}=3.8 \text{ kpc}$, the pitch angle $i=12^\circ.5$, and the normalizing radius $R_n=8.0 \text{ kpc}$. These values are mostly taken from Junqueira et al. (2013). We included two pairs of an $m=2$ spiral, which are separated by different phase angles $\gamma_1=139^\circ.5$ and $\gamma_2=69^\circ.75$. Term m defines the number of the spiral arms. Note that two pairs of an

$m=2$ spiral is not the same as an $m=4$ pattern, which results in nonnegligible Φ_6 components (right panel of Figure 2). We restrict the spiral potential to be important only beyond the solar radius by tapering it off with a Gaussian form inside $R_{\text{sp}}=9 \text{ kpc}$ with $\sigma_{\text{sp}}=1.5 \text{ kpc}$, similar to the approach used in previous studies (e.g., Kim & Ostriker 2006). These values result in a maximum potential perturbation at the solar radius of $\sim 630 \text{ km}^2 \text{ s}^{-2}$, slightly higher than the $\sim 550 \text{ km}^2 \text{ s}^{-2}$ constrained by Eilers et al. (2020). The spiral potential becomes negligible inside $R_{\text{sp}} - 2\sigma_{\text{sp}}=6 \text{ kpc}$, which is close to the R_{CR} of the bar in this study (see the left two panels of Figure 2). The total mass of the spiral is $8.39 \times 10^8 M_\odot$ by solving the Poisson equation for Φ_{sp} , but this may be a lower limit as it is concentrated toward the plane. We rotate the spiral potential with a fixed pattern speed of $\Omega_{\text{sp}}=23.0 \text{ km s}^{-1} \text{ kpc}^{-1}$ as constrained by Junqueira et al. (2015) using open clusters and tested further in Li et al. (2016).

2.4. Bar-spiral Interface

It is well accepted that the central bar rotates faster than the outer spiral arms as can be seen in many simulations (e.g., Quillen et al. 2011; Minchev et al. 2012; Hilmi et al. 2020), although the effect of the bar-spiral interaction on stellar and gas kinematics is still not clear. The bar parameters may vary when interacting with the adjacent spiral arms, but this is simply the beat pattern fluctuation between the bar and spirals. As the bar in the m2m model of P17 is in an approximately steady state, we include a perturbation near the bar ends to mimic the bar-spiral interface:

$$\begin{aligned} \Phi_{\text{bs}}(R, \varphi, z) = & -\zeta_{\text{bs}} R \exp\{-R/\epsilon_{\text{bs}} - |kz|\} \\ & - \frac{R^2}{\sigma_w^2} [1 - \cos(m\varphi - f_m)] \} \\ & \times \exp[-(R - R_{\text{bs}})^2/2\sigma_r^2] \\ & \times \exp[-(\varphi - \varphi_{\text{bs}})^2/2\sigma_\varphi^2]. \end{aligned} \quad (8)$$

This is a tapered spiral arm potential in the R and φ directions, similar to that in Li et al. (2016). Terms $f_m(R)$ and k are defined by Equations (6) and (7). We adopt $m=2$, $R_n=8 \text{ kpc}$, $\gamma=36^\circ$, and $i=42^\circ$, resulting in a shape that smoothly transitions from spirals into the bar ends. Other parameters are $\zeta_{\text{bs}}=1300.0 \text{ km}^2 \text{ s}^{-2} \text{ kpc}^{-1}$, $\epsilon_{\text{bs}}=3.8 \text{ kpc}$, and $\sigma_w=1.5 \text{ kpc}$. The two Gaussian functions have $R_{\text{bs}}=5.5 \text{ kpc}$, $\varphi_{\text{bs}}=12^\circ$ and 192° (corresponding to the two ends of the bar), $\sigma_r=0.5 \text{ kpc}$, and $\sigma_\varphi=5^\circ$. The above parameters are chosen to mimic a tail-like potential around the bar ends that connects the bar with the outer spirals (see Figure 2). By using such a preselected functional form with arbitrarily selected parameters, we would like to first understand how gas responds to a ‘‘tailed’’ barred potential, rather than model a realistic bar-spiral coupling system. The total mass of this component is $4.43 \times 10^7 M_\odot$ by solving the Poisson equation for Φ_{bs} .

In the current paper we assume this perturbation co-rotates with the bar for simplicity. We will see in Section 7.2 that the bar-spiral interface is important to reproduce the observed velocities of HMSFRs around the bar end.

2.5. Modification of the Rotation Curve

Recent studies from both gas (e.g., Reid et al. 2019) and stars (e.g., Eilers et al. 2019; McGaugh 2019) have shown that the circular rotation velocity of the Milky Way reaches

$v \sim 230 \text{ km s}^{-1}$ at $R \sim 4\text{--}5 \text{ kpc}$ and then becomes relatively flat beyond this radius. The m2m model from P17 has a slightly lower rotation velocity around this region. We therefore add an extra radial force to shift the rotation curve as follows:

$$F_{R,\text{pl}}(R, \varphi) = \begin{cases} -\frac{\Delta v}{R} \frac{R - R_i}{R_m - R_i} \\ \times (\Delta v \frac{R - R_i}{R_m - R_i} + 2v_{\text{pl}}), & R_i(\varphi) \leq R < R_m \\ -\frac{\Delta v}{R} \frac{R - R_f}{R_m - R_f} \\ \times (\Delta v \frac{R - R_f}{R_m - R_f} + 2v_{\text{pl}}), & R_m \leq R < R_f \\ 0, & \text{otherwise} \end{cases} \quad (9)$$

with $R_i(\varphi)$ defined as:

$$R_i(\varphi) = \frac{3 \text{ kpc}}{\sqrt{[1 - (e \cos \varphi)^2]}}. \quad (10)$$

Equation (9) corresponds to adding a linearly rising segment in the rotation curve between R_i and R_m , and a linearly declining segment between R_m and R_f with the same amount of velocity shift Δv . The total mass of the Galaxy is therefore unaffected, since this modification only rearranges the mass distribution between R_i and R_f . We adopt $\Delta v = 15 \text{ km s}^{-1}$, $v_{\text{pl}} = 190 \text{ km s}^{-1}$, $R_m = 5.5 \text{ kpc}$, and $R_f = 7.5 \text{ kpc}$. R_i is set to be an ellipse with $e = 0.6$ to avoid the central bar region. The semimajor axis of the ellipse is 3.75 kpc and the semiminor axis is 3.0 kpc . The corresponding gravitational potential Φ_{pl} is numerically computed based on $F_{R,\text{pl}}$.

2.6. Parameter Space

Although there are quite a lot of parameters listed in Section 2, many of them are fixed in the current study as these are relatively well constrained by observations and other studies (e.g., the shape of the NSD and the large-scale spirals). We run about 60 models to see how gas evolves in different potentials for different bar pattern speeds, mainly focusing on investigating Ω_b in the range $35.0\text{--}42.5 \text{ km s}^{-1} \text{ kpc}^{-1}$ and the velocity shift Δv of Equation (9) in the range $0\text{--}30 \text{ km s}^{-1}$. We then define the models that can best reproduce observations in this 2D parameter space as our fiducial models. We also test different parameters of the bar-spiral interface described by Equation (8) in the fiducial models. The parameters varied are ζ_{bs} in the range $0\text{--}2000 \text{ km}^2 \text{ s}^{-2} \text{ kpc}^{-1}$, R_{bs} in the range $4.0\text{--}6.0 \text{ kpc}$, and i in the range $30^\circ\text{--}50^\circ$. More details of different models can be found in Section 6 and the Appendix.

3. Constraints from Observations

3.1. The (l, v) Diagram

We compare the features in (l, v) space with those identified in observed HI and CO from Reid et al. (2016) together with Rodriguez-Fernandez & Combes (2008), and compare terminal velocities with measurements from McClure-Griffiths & Dickey (2007), Burton & Liszt (1993), and Clemens (1985), as in Li et al. (2016).

To obtain the (l, v) diagram of the models, we assume the Sun is located at $(x, y, z) = (0 \text{ kpc}, -8.15 \text{ kpc}, 0.025 \text{ kpc})$, with

a circular velocity of the local standard of rest (LSR) $v_{\text{LSR}} = 236 \text{ km s}^{-1}$. We also consider the peculiar motions of the Sun with respect to the LSR as $(U, V, W) = (10.6, 10.7, 7.6) \text{ km s}^{-1}$. These values are taken from Reid et al. (2019; see also Schönrich et al. 2010; Bland-Hawthorn & Gerhard 2016; Gravity Collaboration et al. 2019). The bar angle to the Sun $-GC$ line is fixed at 28° (Portail et al. 2017). We then calculate the Galactic longitude l and line-of-sight velocity v_{LOS} in each cell of the simulation grid based on the solar position and the gas velocity \vec{v} . The results are binned onto an (l, v) grid weighted by the gas density ρ . In the current study we do not consider radiative transfer effects, but just assume that the observed flux intensity is proportional to the gas density. The (l, v) grid for the simulation has a bin size of $\Delta l = 0.6^\circ$ and $\Delta v = 3 \text{ km s}^{-1}$.

3.2. HMSFRs

The (l, v) diagram contains the information of directions and LOS velocities only. We further consider the positions and tangential motions of the HMSFRs with high-precision VLBI data (Reid et al. 2014, 2019; VERA Collaboration et al. 2020) as constraints. A successful gas dynamical model should explain the (l, v) diagram and the 3D motions of the observed HMSFRs simultaneously. For the current study we select the HMSFRs from Reid et al. (2019) that lie within $|z| \leq 0.1 \text{ kpc}$ from the Galactic plane and $R \leq 12 \text{ kpc}$ from the GC to constrain our gas models. Furthermore, we only consider the HMSFRs that have distance uncertainties of less than 0.5 kpc . This selection results in a sample of 135 HMSFRs. As the gas in our models cannot form stars (or HMSFRs), we then interpolate our models and compare the gas properties at the same locations with the observed HMSFRs.

4. Numerical Scheme

The simulations are performed using a modified version of the Athena++ code⁶ (White et al. 2016; Stone et al. 2019, 2020). We adopt a uniform Cartesian grid with $2048 \times 2048 \times 21$ cells covering a simulation box of $(24 \times 24 \times 0.2) \text{ kpc}$ along the (x, y, z) directions, respectively. The corresponding resolution is roughly 10 pc . The typical time step for integration is $\Delta t \sim 1.4 \times 10^3 \text{ yr}$. Other options adopted are piecewise linear reconstructions, the roe Riemann solver (Roe 1981), and the outflow boundary condition.

We essentially study the response of a thin gas disk under a realistic bar-spiral Milky Way potential described by Equation (1). The initial gas disk has a density profile of

$$\rho_{\text{gas}}(R, z) = \frac{\Sigma_{\text{g}}}{2z_{\text{gas}}} \exp(-R/R_{\text{gas}}) \text{sech}^2(z/z_{\text{gas}}), \quad (11)$$

where $\Sigma_{\text{g}} = 71.1 M_{\odot} \text{ pc}^{-2}$, $R_{\text{gas}} = 4.8 \text{ kpc}$, and $z_{\text{gas}} = 130 \text{ pc}$. The corresponding gas surface density at the solar radius ($R_{\odot} = 8.15 \text{ kpc}$) is $\Sigma_{\text{g},0} = 13 M_{\odot} \text{ pc}^{-2}$, consistent with Bovy & Rix (2013) and P17. The total mass of the gas disk is $\sim 10^{10} M_{\odot}$.

We start with gas on circular orbits in an axisymmetrized potential, which is obtained by azimuthally averaging Φ_{gal} . The non-axisymmetric components are linearly ramped up during the first 100 Myr to avoid transients, similar to previous studies (e.g., Kim et al. 2012; Sormani et al. 2015a).

⁶ <https://princetonuniversity.github.io/athena/>

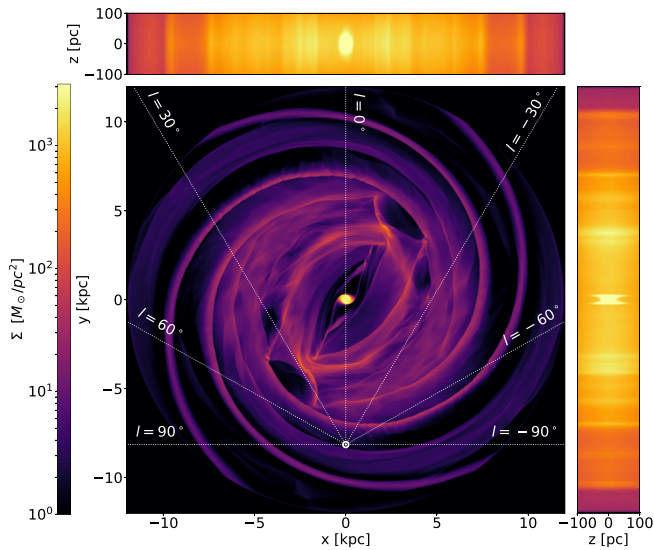


Figure 3. Integrated gas surface density along three directions of our fiducial model with $\Omega_b = 37.5 \text{ km s}^{-1} \text{ kpc}^{-1}$ at $t = 440 \text{ Myr}$. Note the scale along the z direction is not the same as for x and y to highlight the fine details in the vertical direction. The Sun is located at $(0 \text{ kpc}, -8.15 \text{ kpc})$ as indicated by the solar symbol. Seven white dotted lines represent different Galactic longitude directions (0° , $\pm 30^\circ$, $\pm 60^\circ$, and $\pm 90^\circ$).

We adopt an isothermal equation of state (EoS) and assume an *effective* isothermal sound speed $c_s = 10 \text{ km s}^{-1}$, as in previous studies (e.g., Fux 1999; Rodriguez-Fernandez & Combes 2008; Kim et al. 2012; Ridley et al. 2017). This sound speed makes the gas transition from the x_1 to x_2 orbits happen in places consistent with observations (Sormani et al. 2015a). The corresponding temperature is 15,422 K assuming a mean molecular weight of 1.273 (e.g., Glover & Clark 2012). Note this effective sound speed reflects the velocity dispersion of gas clouds in the Galactic disk (around 10 km s^{-1} ; see Burton 1976; Walter et al. 2008; Tamburro et al. 2009) instead of a microscopic temperature. The isothermal EoS enables us to focus more on the effects of the asymmetric potential on gas flows by neglecting microscopic physics such as cooling, star formation, and stellar/supernova feedback. It also helps to explore a larger parameter space of the potential, as the current simulation setup is not very computationally expensive (it takes about 3 days to evolve one model to 500 Myr using 256 Intel Xeon(R) Gold 6240 cores). The self-gravity of gas is neglected. We regard our isothermal simulations as a first-order approximation to the observed cold gas in the Milky Way. We also present the models with different c_s in Figures A2 and A3. The caveats of this assumption are discussed in Section 8.3.

5. Overall Gas Morphology and Kinematics

Figure 3 shows the integrated gas surface density in our fiducial model with $\Omega_b = 37.5 \text{ km s}^{-1} \text{ kpc}^{-1}$ and $\Delta v = 15 \text{ km s}^{-1}$. We chose the location of the Sun (white solar symbol in the plot) based on a fixed bar angle to the Sun–GC line of 28° , which is well constrained by P17. This snapshot is taken when the spirals roughly finish one rotation period in the bar co-rotating frame, i.e., $T_p = 2\pi/\Delta\Omega \approx 440 \text{ Myr}$, where $\Delta\Omega = \Omega_b - \Omega_{\text{sp}}$. As we initialized the spiral potential based on the observed spiral phase angles in Reid et al. (2019; see Figure 2), both the bar and spiral arms have appropriate

locations relative to the Sun around $T_p = 440 \text{ Myr}$ as the initial state.

In the central $\sim 200 \text{ pc}$ of the plot there is a high-density nuclear gas ring/disk, which corresponds to the observed Central Molecular Zone (CMZ). Two strong shocks emerge from the central disk and roughly extend to the bar ends. This is a typical gas flow pattern in a rotating barred potential (e.g., Athanassoula 1992; Kim et al. 2012; Li et al. 2015; Sormani et al. 2015a). At a larger radius an elliptical gaseous ring surrounding the bar ends around $l \sim \pm 30^\circ$. This type of gas ring around the bar, dubbed an “inner ring,” has also been commonly found in external barred galaxies (de Vaucouleurs 1959; Sandage 1961; Combes 1996; Kormendy & Bender 2019) and in cosmological hydrodynamical simulations (Grand et al. 2017; Fragkoudi et al. 2020). A few gas spurs connect the ring to the spiral arms in the outer disk regions. The Sun is located slightly inside the Local arm, which also shows a well-defined spiral shape in the plot. These gas structures could have also been identified from the edge-on view as ridge lines.

Figure 4 presents a clearer view of the gas in different regions and their corresponding kinematics in the (l, v) space. Note in the top row the bar is always aligned with the x -axis for better illustration. We separate the gas flow pattern into three parts: the bar-driven inflows (left column), the “inner ring” around the bar (middle column), and the large-scale outer spirals (right column). The flow in the left column is highly noncircular, and the gas can reach an LOS velocity of $\geq 200 \text{ km s}^{-1}$ since it flows in streams along the shocks. The typical LOS velocities in this region are around $100\text{--}200 \text{ km s}^{-1}$. The CMZ in our model corresponds to the parallelogram in the (l, v) space within $|l| \leq 2^\circ$. The elliptical gas “inner ring” surrounding the bar in the middle column is composed of four spiral segments, and they form four lines in the (l, v) space with typical LOS velocities of around $50\text{--}100 \text{ km s}^{-1}$. The near and far 3 kpc arms in our model correspond to the top and bottom lines. The two gas spurs at the bar ends can be seen in the (l, v) space as the kinks around $l \sim 30^\circ$ and -15° , respectively. The outer spiral arms in the right columns are shown by the high-density ridges in the (l, v) space with low LOS velocities of $\sim 10\text{--}50 \text{ km s}^{-1}$. A combined figure with observations included is presented in Figure 5. We explain in the following sections how we constrain the bar pattern speed, together with the Galactic potential, by directly comparing these structures to observations.

6. Bar Pattern Speed and the Rotation Curve from Gas Dynamics

The (l, v) diagrams of the models with four bar pattern speeds ($\Omega_b = 35.0, 37.5, 40.0,$ and $42.5 \text{ km s}^{-1} \text{ kpc}^{-1}$), three rotation curve shifts (Δv from Equation (9) with 0, 15, and 30 km s^{-1}), and the presence (or not) of the bar-spiral interface Φ_{bs} , are summarized in Figure 6. We only plot the terminal velocity (i.e., the envelope of the (l, v) diagram), the 3 kpc arms, and the forbidden velocity region in order to highlight the differences between the models in the (l, v) space. The 3 kpc arms are the bar-driven spirals discussed in Section 5, and the forbidden velocity regions are defined as ($l \leq 0^\circ, v_{\text{LOS}} \geq 0 \text{ km s}^{-1}$) and ($l \geq 0^\circ, v_{\text{LOS}} \leq 0 \text{ km s}^{-1}$) where gas on a circular orbit is not expected to appear. The 3 kpc arms and forbidden velocities are closely related to the bar pattern speed (see also Sormani et al. 2015c), while the terminal velocity is both

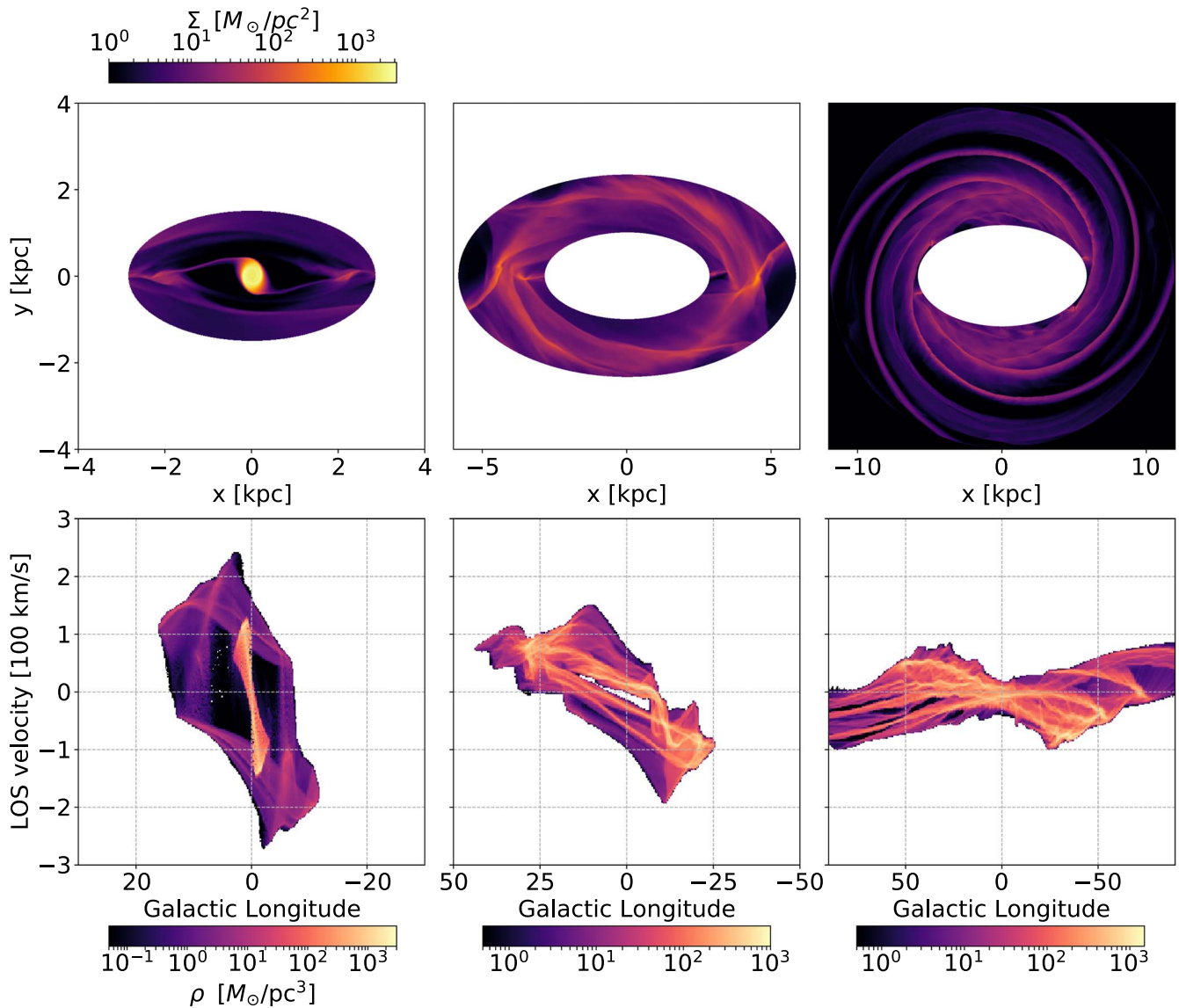


Figure 4. Gas surface density plots (top row) and the corresponding (l, v) diagrams (bottom row) of the fiducial model with $\Omega_b = 37.5 \text{ km s}^{-1} \text{ kpc}^{-1}$ in different regions. From left to right: gas flows inside an ellipse with a semimajor axis of 2.85 kpc and a semiminor axis of 1.5 kpc. The CMZ can be seen as the high-density nuclear ring/disk in the top panel and in the parallelogram in the bottom panel within $|l| \leq 2^\circ$; gas flows outside the previous ellipse but inside the second ellipse with a semimajor axis of 5.83 kpc and a semiminor axis of 3.5 kpc; gas flows outside the second ellipse.

associated with the bar/spiral and the shape/amplitude of the rotation curve.

Figure 6 shows the 3 kpc arms (blue solid lines), the forbidden velocity region (green solid line), and the terminal velocity (yellow solid lines) in our models with parameters mentioned above. The corresponding features from observations are shown by the black lines. The model parameters are listed on the bottom left of each panel. Note the 3 kpc arms in the models are manually extracted from the (l, v) diagram in order to avoid contamination from other features. We see from top to bottom that the 3 kpc arms become more tilted, and the forbidden velocity region is less pronounced compared to observations with a higher Ω_b . We only plot the forbidden velocity on the negative longitude as the data are limited on the other side. The terminal velocity curves in the leftmost column are clearly below the observed one within $20^\circ \lesssim |l| \lesssim 40^\circ$, which motivates us to shift the rotation curve in this region. This also implies that the disk mass inside the bar region may

be underestimated in the original P17 potentials. The models with $\Delta v = 15 \text{ km s}^{-1}$ seem to be enough to explain the observed terminal velocity, while the models with $\Delta v = 30 \text{ km s}^{-1}$ produce higher curves beyond $|l| \sim 40^\circ$. We also find that including the bar-spiral interface does not significantly affect the 3 kpc arms and the forbidden velocity, but it helps to create an obvious tangent at around $l = 30^\circ$, which better agrees with observations.

To quantify the differences between models, we define $\eta_{3\text{kpc}}$ as the areas between the 3 kpc line segments in the models and observations, i.e., it is the space enclosed by the blue solid lines and dashed black lines in Figure 6. Area η_{forb} is defined in a similar way for the forbidden velocity line segment. For the terminal velocity curves, we use the Dynamic Time Warping (DTW) distance η_{enve} between models and observations to capture the trend of tangent variations along Galactic longitude. The calculations are done with the help of the `similarity-measures` package (Jekel et al. 2019) in `python`. The results

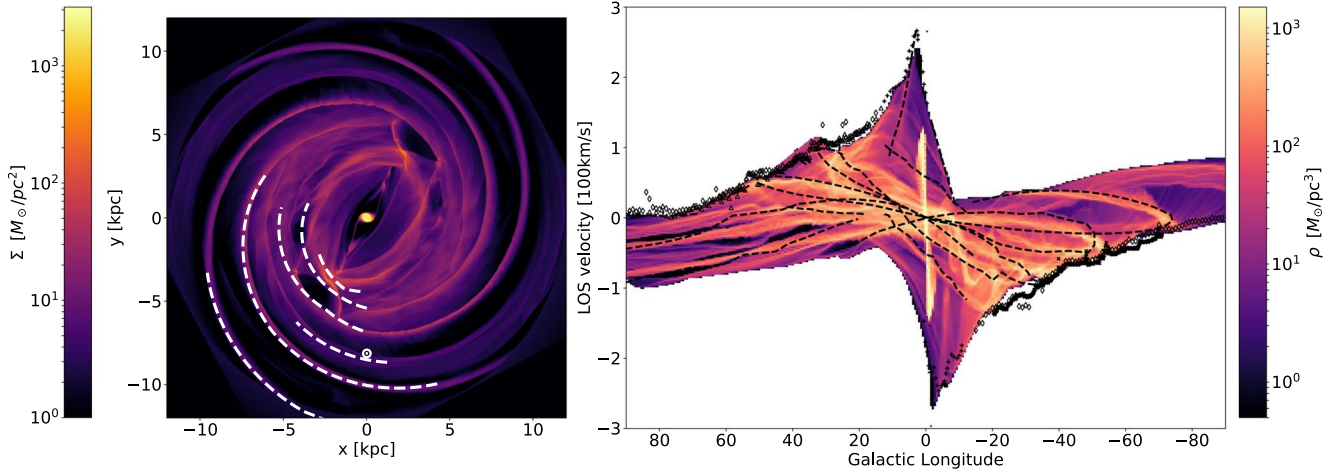


Figure 5. Our fiducial gas model with $\Omega_b = 37.5 \text{ km s}^{-1} \text{ kpc}^{-1}$. Left panel: the gas surface density map. The solar symbol represents the Sun’s location at (0 kpc, -8.15 kpc). The bar major axis has an angle of 28° with respect to the Sun–GC line. The white dashed lines show spiral arm locations from Reid et al. (2019). Right panel: the (l, v) diagram of the model. Dashed lines represent various features identified in Reid et al. (2016) and Rodriguez-Fernandez & Combes (2008). The limits of the color bar are chosen to highlight most of the features. The black crosses, diamonds, and plus signs are H I terminal velocities adopted from McClure-Griffiths & Dickey (2007), Fich et al. (1989), and Burton & Liszt (1993), respectively. The open triangles show the CO terminal velocities from Clemens (1985) at positive longitudes.

are listed on the upper right of each panel, and a smaller η means a better match for a certain feature. We find that our gas models prefer a bar pattern speed within $\Omega_b = 37.5\text{--}40 \text{ km s}^{-1} \text{ kpc}^{-1}$ based on the diagnostics of $\eta_{3\text{kpc}}$ and η_{forb} , as these parameters reach a local minimum in this Ω_b range. The terminal velocity prefers a rotation curve shift around $\Delta v = 15 \text{ km s}^{-1}$ based on η_{enve} . These selection criteria lead to the two fiducial models (highlighted by the cyan dashed box) mentioned in the previous sections. The corresponding R_{CR} for these two models is in the range of 6.0–6.4 kpc as shown in Figure 1. These values are also consistent with some of the previous gas dynamical models (e.g., Rodriguez-Fernandez & Combes 2008; Sormani et al. 2015c) and the independent stellar kinematics measurements in the bulge (e.g., Clarke et al. 2019; Sanders et al. 2019).

Recent work by Chiba et al. (2021) suggested the Galactic bar may currently be in a decelerating phase with a slowing rate $\dot{\Omega}_b = -4.5 \pm 1.4 \text{ km s}^{-1} \text{ kpc}^{-1} \text{ Gyr}^{-1}$. The authors also concluded models with a constant Ω_b may give qualitatively wrong conclusions. We argue that our pattern speed measurement is not sensitive to a small bar slowing rate, as the response of gas flows to the bar potential is quite rapid. In our models the gas reaches a quasi-steady state within about two bar rotation periods, i.e., $\sim 300 \text{ Myr}$ for $\Omega_b = 37.5\text{--}40 \text{ km s}^{-1} \text{ kpc}^{-1}$. Adopting $\dot{\Omega}_b = -4.5 \text{ km s}^{-1} \text{ kpc}^{-1} \text{ Gyr}^{-1}$, this yields an uncertainty of $1.35 \text{ km s}^{-1} \text{ kpc}^{-1}$, which is not significant. We have also tested a decelerating bar with $\Omega_b(t) = 39.5 - 4 \times (t/\text{Gyr})$, and the resulting (l, v) diagram is almost indistinguishable compared to Figure 5. By contrast, Hilmi et al. (2020) predicted the Ω_b and the bar length may change by 20% due to the bar-spiral interaction within one bar rotation. This timescale is shorter than that required by gas to reach a quasi-steady state, as such our Ω_b measurements can only be regarded as a time-averaged value. However, we note that the spirals connected with the bar seem quite massive in Hilmi et al. (2020), which can be sufficient to affect the bar dynamics. For a comparison, the mass of the bar-spiral interface used in our model is $\sim 4.43 \times 10^7 M_\odot$. This mass is enough to explain the large peculiar motion of HMSFRs around the bar end (see Section 7.2 and Figure A1), but is only $\sim 0.24\%$ of the total bar mass ($1.88 \times 10^{10} M_\odot$ in P17), and $\sim 0.82\%$ of the long bar

mass ($5.4 \times 10^9 M_\odot$ in P17; see also Wegg et al. 2015). The total mass of the four arm spiral plus the bar-spiral interface is $88.83 \times 10^8 M_\odot$, which is $\sim 4.69\%$ of the total bar mass. Such a mass contrast makes it unlikely that the adopted bar-spiral interface can dramatically affect Ω_b . Future investigations are required to better constrain $\dot{\Omega}_b$ in the short and long term for the Milky Way’s bar.

7. Mass Distribution in Different Regions

The gas morphology and kinematics provide key information for the underlying mass distribution, and could help us to better understand the large-scale structures of the Galaxy. We use our fiducial model with $\Omega_b = 37.5 \text{ km s}^{-1} \text{ kpc}^{-1}$ as an example to discuss its gas properties and the related mass components in three different regions of the MW.

7.1. Nuclear Stellar Disk and Central Molecular Zone

The NSD is a flattened stellar structure located in the central $R \leq 150\text{--}200 \text{ pc}$ of the Galaxy, with a scale length of $\sim 100\text{--}200 \text{ pc}$ and a scale height of $\sim 45 \text{ pc}$ (Launhardt et al. 2002; Nishiyama et al. 2013; Schönrich et al. 2015; Gallego-Cano et al. 2020). The gaseous counterpart of the NSD is probably the CMZ, which is a high-density gas ring/disk with a radius of $\sim 200 \text{ pc}$ (Molinari et al. 2011; Henshaw et al. 2016). Pioneering works led by Binney et al. (1991) interpret the CMZ as cold gas switching from x_1 orbits to x_2 orbits, while for warm gas the x_2 orbits would not be occupied (Englmaier & Gerhard 1997). The CMZ can therefore be regarded as a counterpart to circumnuclear (or nuclear) rings in external barred galaxies (Comerón et al. 2010; Li et al. 2015). The latest studies that include more physics can form structures reminiscent of the CMZ and NSD in a barred Milky Way model (e.g., Seo et al. 2019; Baba & Kawata 2020; Tress et al. 2020; Sormani et al. 2020b).

The gas kinematics in the Galactic central region offer tight constraints on the NSD properties. A more massive and/or compact NSD may result in a steeper rise in LOS velocity compared to observations, and vice versa (see Li et al. 2020). We show in Figure 7 that a central NSC+NSD mass of

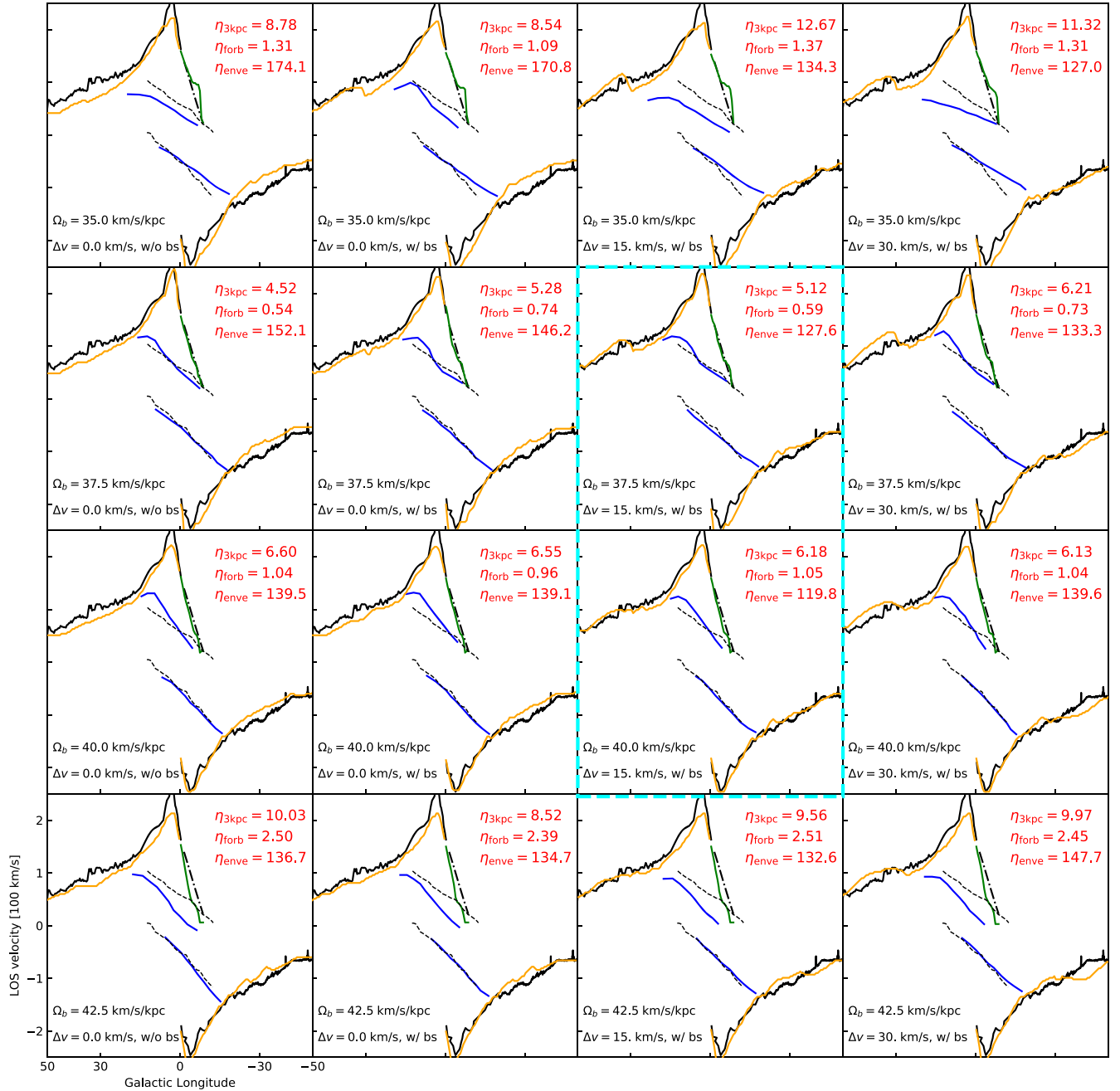


Figure 6. Comparison between models. From left to right: gas model in the potential with neither the bar-spiral interface nor the rotation curve shift; gas model with the bar-spiral interface but without the rotation curve shift; gas model with the bar-spiral interface and the rotation curve shift with $\Delta v = 15 \text{ km s}^{-1}$; and gas model with the bar-spiral interface and the rotation curve shift with $\Delta v = 30 \text{ km s}^{-1}$. From top to bottom: gas model with $\Omega_b = 35, 37.5, 40,$ and $42.5 \text{ km s}^{-1} \text{ kpc}^{-1}$. In each panel, the black solid lines represent the terminal velocities from Clemens (1985), Fich et al. (1989), Burton & Liszt (1993), and McClure-Griffiths & Dickey (2007); the black dashed lines represent the 3 kpc arms from Reid et al. (2016); and the black dotted–dashed line represents the forbidden velocity from Rodriguez-Fernandez & Combes (2008). The yellow, blue, and green solid lines are the corresponding features in the models. The differences between the model and the observations for these three features are listed on the upper right of each panel. The two fiducial models are highlighted by the cyan dashed box.

$7.5 \times 10^8 M_\odot$ can generate a gas disk with a similar size and kinematics as for the observed CMZ. The figure shows the gas surface density and the (l, v) diagram in the central 500 pc of our fiducial model with $\Omega_b = 37.5 \text{ km s}^{-1} \text{ kpc}^{-1}$. The gas ring/disk (or a pair of tightly wound spirals) at a radius of ~ 200 pc in the left panel corresponds to the observed CMZ, similar to previous simulations (e.g., Kim et al. 2011; Ridley et al. 2017; Armillotta et al. 2019). The (l, v) diagram of the model is shown in the middle panel. The black dashed–dotted line denotes the circular rotation curve of the model. The envelope

of the gas (l, v) diagram roughly matches the rotation curve, suggesting gas motions can be used to trace the central potential. The spikes with low velocities at the gas above the midplane. The slightly up-down asymmetry of the (l, v) diagram in the model is due to the $\sim 10 \text{ km s}^{-1}$ inward solar motion mentioned in Section 3.1; this asymmetry is probably also noticeable in the C II observation (blue shaded region). The NH_3 data (small blue points) reach $v_{\text{LOS}} = 90\text{--}110 \text{ km s}^{-1}$ around $l \sim 1^\circ$, and the model follows a similar pattern, indicating that the NSD mass profile we adopt is reasonable. The asymmetric

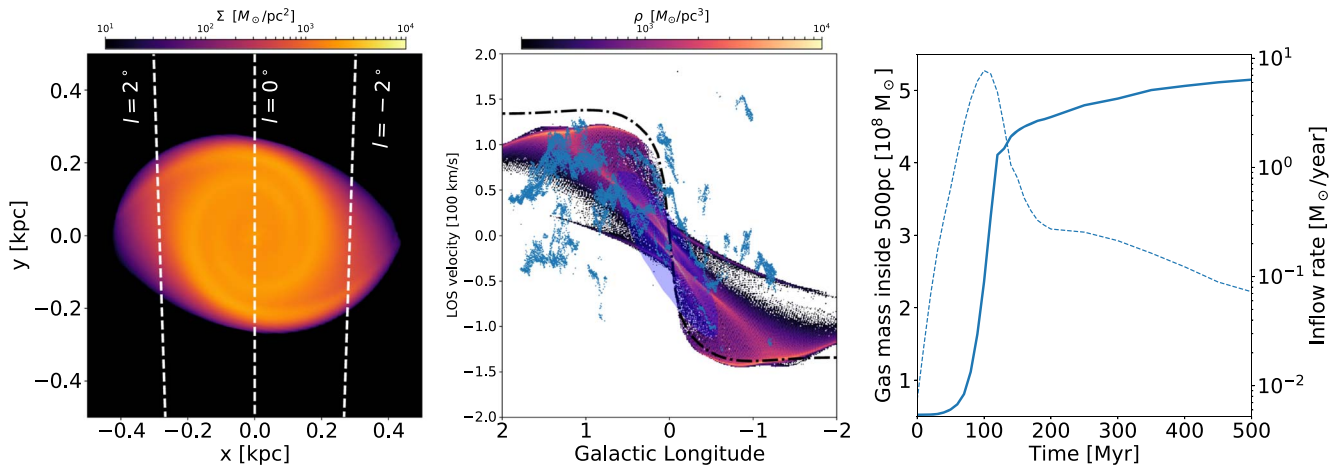


Figure 7. Zoom-in view of the central region in the fiducial model with $\Omega_b = 37.5 \text{ km s}^{-1} \text{ kpc}^{-1}$ at $t = 440 \text{ Myr}$. The limits of the color bar are adjusted compared to Figure 5 to better visualize the high-density region. Left panel: the gas surface density map. Middle panel: the corresponding (l, v) diagram. We interpolate our model with a 2 pc resolution within 1 kpc to better show the central features. The bin sizes are $\Delta l = 0^\circ 01$ and $\Delta v = 1.0 \text{ km s}^{-1}$. The black dashed-dotted line indicates the circular rotation velocity adopted in the model. The blue shaded region shows the observations of C II obtained from Langer et al. (2017). The small blue dots are NH_3 observations from the HOPS survey after processing with SCOUSE (Henshaw et al. 2016; Longmore et al. 2017). Right panel: accumulated gas mass inside 500 pc as a function of simulation time (solid line), and the corresponding mass inflow rate (dashed line).

NH_3 distribution with respect to $l=0^\circ$ is probably due to the transient instabilities developed by the inflowed gas (Wada & Koda 2004; Sormani et al. 2018). These instabilities may also help explain the velocity drop in NH_3 from $\sim 100 \text{ km s}^{-1}$ to $\sim 50 \text{ km s}^{-1}$ in the range of $l \sim 1^\circ$ to 2° (e.g., Li et al. 2020). It is also possible that the drop is created by collisions between gas streams moving at different speeds along the shocks (Sormani et al. 2019). Such a velocity drop is even steeper than Keplerian, and thus it must be highly noncircular, and it is difficult to use this drop to constrain the mass distribution. In general, we find the gas kinematics in the CMZ of our model agree with a $\sim 7 \times 10^8 M_\odot$ NSD in the central $|l| = 2^\circ$. Interestingly, P17 obtained a dynamical central mass of $\sim 2 \times 10^9 M_\odot$ based on stellar proper motions in the central region. This is about three times larger than in our model and Sormani et al. (2020a). A likely reason for this discrepancy is that the NSD mass in P17 was constrained by OGLE proper motions at higher latitudes ($|b| > 2^\circ$), reflecting an enclosed mass on larger scales. Further observations like JASMINE (Gouda 2012) and GaiaNIR (Hobbs et al. 2019) will provide more insight on the origin and mass of the NSD in our Galaxy.

The right panel of Figure 7 shows the enclosed mass in the central 500 pc (solid line) and the corresponding mass inflow rate (dashed line) as a function of time. It is clear that most inflow happens in the first 100 Myr, even less than one bar rotation period. After $\sim 200 \text{ Myr}$ the mass inflow rate becomes relatively small. The short inflow timescale is also revealed in the star formation history (SFH) derived by Nogueras-Lara et al. (2019). The inflow rate at $t \gtrsim 400 \text{ Myr}$ falls below $\sim 0.1 M_\odot \text{ yr}^{-1}$, because gas is not replenished (or is done so slowly by the outer spiral arm) inside the bar region of our isolated models. For a comparison, the mass inflow rate to the CMZ region based on an observational estimation gives $\sim 0.8 - 2.7 M_\odot \text{ yr}^{-1}$ (Sormani & Barnes 2019; Hatchfield et al. 2021). The large observed inflow rate may be related to the recent disk perturbation due to (massive) satellites (e.g., Antoja et al. 2018; Bland-Hawthorn et al. 2019; Laporte et al. 2019; Li & Shen 2020), or possibly due to the infalling gas clouds from the Molecular Ring reservoir perturbed by spiral arms (e.g., Bissantz et al. 2003). At the end of our simulation

($t = 500 \text{ Myr}$) the enclosed gas mass reaches $5.15 \times 10^8 M_\odot$. This suggests the bar is able to drive around 5% of the initial gas disk ($1.0 \times 10^{10} M_\odot$) into the center if there is little gas replenishment inside the bar region. However, the observed mass of molecular gas in the CMZ is around $\sim 3-7 \times 10^7 M_\odot$ (Launhardt et al. 2002; Molinari et al. 2011), which is about an order of magnitude lower than that in the model. This discrepancy can be understood, as most dense gas would turn into stars and then become part of the NSD, and a fraction of the accumulated gas would be ejected by stellar feedback, but these processes are not yet included in the current model. In addition, magnetic fields (Mangilli et al. 2019) and turbulence (Salas et al. 2020) may also be important in modeling the detailed gas properties in the CMZ. We would like to study these effects and make a more careful comparison with the CMZoom survey (Hatchfield et al. 2020) in a future work.

7.2. Bar-spiral Interface and Molecular Ring

Reid et al. (2019) found that their observed HMSFRs have significant noncircular motions ($\sim 50 \text{ km s}^{-1}$) in a portion of the Perseus arm and near the bar ends. These large peculiar motions are believed to be related to the dynamics of the Galactic bar and spiral arms. Baba et al. (2018) proposed that a disrupting spiral arm is able to explain the peculiar motions in the Perseus arm, while no previous models can qualitatively reproduce the large peculiar motions at the bar ends.

We show in Figure 8 that our model can explain the observed peculiar motions at the bar end by introducing a bar-spiral interface term described by Equation (8). The left panel of Figure 8 plots the gas surface density of our fiducial model with $\Omega_b = 37.5 \text{ km s}^{-1} \text{ kpc}^{-1}$; the overlaid gray points are the observed HMSFRs described in Section 3.2. Equation (8) is mainly responsible for generating the nearly vertical gas spur (shock) at $x \sim -2 \text{ kpc}$ and $y \sim -4 \text{ kpc}$ to -6 kpc (and its counterpart at the other side of the Galaxy). The observed HMSFRs seem to be preferentially located around this spur, implying that it is a possible birth place. The peculiar motions of the observations and the model are shown in the middle and right panels of Figure 8, respectively. Since our model does not

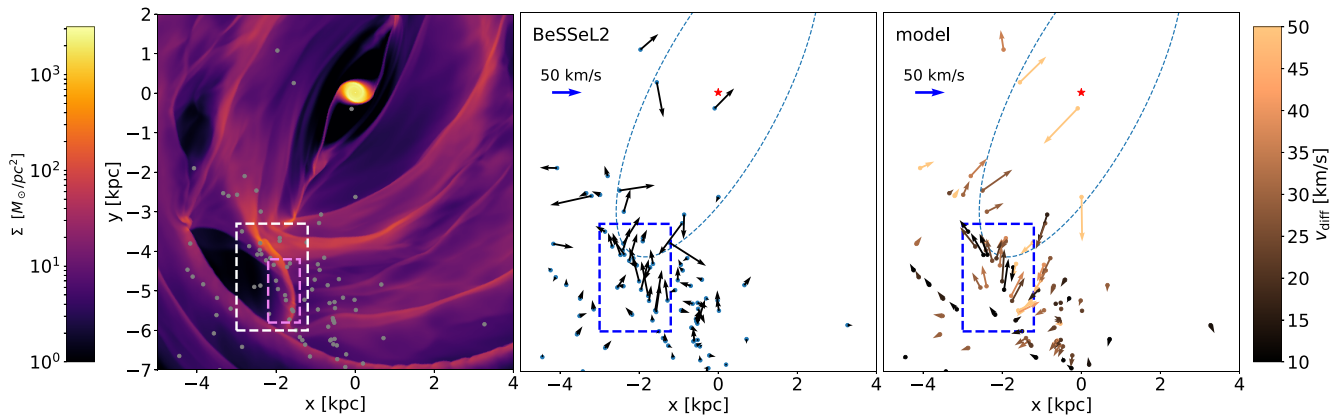


Figure 8. Comparison between our fiducial model with $\Omega_b = 37.5 \text{ km s}^{-1} \text{ kpc}^{-1}$ and BeSSeL2 results. Left panel: the gas surface density overlaid with the locations of observed HMSFRs (gray dots) from Reid et al. (2019). The white dashed box highlights the region of the observed HMSFRs with large peculiar motions. The gas spur has a mass of $1.94 \times 10^7 M_\odot$ inside the purple dashed box. Middle panel: noncircular (peculiar) motions of the HMSFRs in BeSSeL2. The blue dashed curve roughly outlines the shape of the bar. The blue dashed box shows the same region as the white one in the left. A 50 km s^{-1} velocity vector is shown for reference at the upper left corner. The red star indicates the GC. Right panel: noncircular motions at the same locations in the model. The color of the arrow represents the velocity difference Equation (12) between the model gas and the observed HMSFRs.

include mechanisms to form HMSFRs, we assume the underlying gas flows have similar kinematics to the HMSFRs and thus plot the peculiar motion of the model gas at the location of the observed HMSFRs. The peculiar motions are calculated by subtracting the circular rotation velocity (Figure 1) from the 3D velocity for both our model and observations. The color of the arrows in the right panel quantifies the velocity difference v_{diff} between the model and observations for each HMSFRs, which is defined as:

$$v_{\text{diff}} = \sqrt{(\tilde{v}_{R,\text{obs.}} - \tilde{v}_{R,\text{model}})^2 + (\tilde{v}_{\phi,\text{obs.}} - \tilde{v}_{\phi,\text{model}})^2}, \quad (12)$$

where \tilde{v}_R and \tilde{v}_ϕ are the peculiar motions along the R and ϕ directions. Although there are still discrepancies for a few individual points, the overall patterns of the model and data are similar, with a typical v_{diff} of around 20 km s^{-1} .

We focus on the 26 HMSFRs inside the blue dashed box in the middle and right panels where the local potential is more affected by Equation (8). The HMSFRs in this region have a mean \tilde{v}_R of -21.5 km s^{-1} and a mean \tilde{v}_ϕ of 8.6 km s^{-1} , while for the same locations our gas model gives -12.0 km s^{-1} and 7.5 km s^{-1} , respectively. In general, gas is moving inwards and is faster than the local circular motion in this region. The reason for such a peculiar motion pattern is due to the bar-spiral interface that creates a local potential minimum around the bar ends. Gas is first accelerated when entering the potential minimum, but as the bar-spiral interface co-rotates with the bar, gas is then trapped around this region and turns into a local shock feature that is nearly radial. Since the post-shock region should be subsonic (in our case $\leq 10 \text{ km s}^{-1}$), the flow becomes mostly radial after passing the shock. The gas is then compressed at the shock front and is prone to the formation of HMSFRs. The model without the bar-spiral interface cannot form such a pattern (see Figure A1). Our results demonstrate that the potential related to the bar-spiral interface may need to be taken into account to study the kinematics of gas and stars in this region. We note the shape and amplitude of the spiral arms are still uncertain around the bar end. In principle, a strong arm with a large pitch angle in this region may also cause similar motions as the bar-spiral interface does, but this may imply a different spiral pattern compared to the BeSSeL observations.

Hilmi et al. (2020) also studied the bar-spiral interaction and proposed that the length of the Milky Way bar may be overestimated by 1–1.5 kpc, and its pattern speed may be underestimated by 5–10 $\text{km s}^{-1} \text{ kpc}^{-1}$ compared to the time-averaged value. The reason they argued is because the Scutum-Centaurus-OSC⁷ arm may be connected to the near half of the bar at present. We find in our configuration that the bar-spiral interface indeed connects the bar and the Scutum arm, but it dominates only the local gas kinematics (i.e., around the bar ends). Other gas features like the 3 kpc arms are largely unaffected by the presence of this feature (e.g., Figure 6). It is possible that the bar-spiral interface needs to be considerably more massive than in our case to alter the bar properties. However, the gas itself in this region may be sufficient to generate a local potential minimum that could explain the observed peculiar motions. The gas mass inside the purple box shown in the left panel of Figure 8 is $1.94 \times 10^7 M_\odot$, which is very close to the mass of the bar-spiral interface ($2.21 \times 10^7 M_\odot$) introduced by Equation (8). Further work is still needed to investigate in more detail the mass distribution around the bar end.

One may wonder to what extent HMSFRs trace the underlying gas flows. This may depend on their lifetime and the ratio of mass density in HMSFRs to the surrounding gas, although these properties may not be easily measured. Reid et al. (2019) found that the observed HMSFRs are relatively concentrated near the high-density gas ridges in the (l, v) diagram, with a typical dispersion of $10\text{--}20 \text{ km s}^{-1}$. Assuming the tangential velocity has a similar scatter, this leads to a total velocity offset of $15\text{--}30 \text{ km s}^{-1}$. The simulations by Baba et al. (2009) suggested a comparable velocity difference between the motions of dense gas and young stars. The overall 135 HMSFRs have an average v_{diff} of 24.5 km s^{-1} compared to our gas model shown in Figure 5, roughly consistent with the above differences. We therefore conclude that HMSFRs probably trace the underlying global gas flows reasonably well. Careful work on the formation of HMSFRs in disk galaxies is required to understand this problem further.

⁷ OSC stands for Outer-Scutum-Centaurus; see the definitions in Reid et al. (2019).

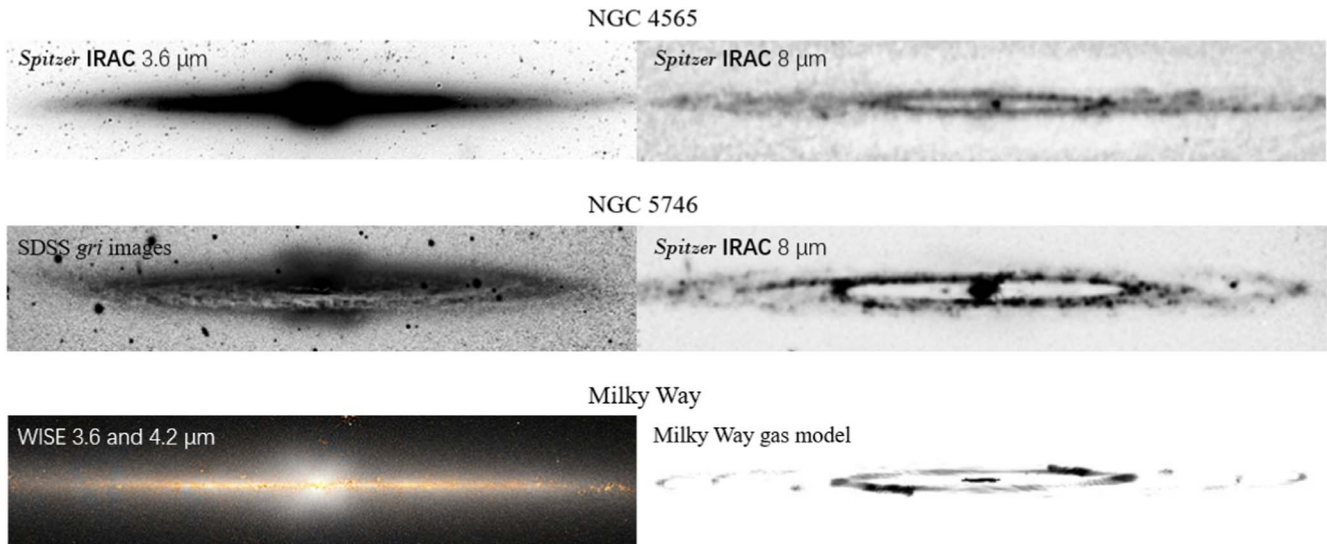


Figure 9. Comparison between our fiducial gas model in Figure 3 and two possible Milky Way analogs. Top row: Spitzer IRAC 3.6 and 8 μm negative images of NGC 4565. Middle row: Sloan Digital Sky Survey *gri* images and Spitzer IRAC 8 μm negative images of NGC 5746. These images are adapted from Kormendy & Bender (2019). Bottom row: Wide-field Infrared Survey Explorer image of the Milky Way from Ness & Lang (2016) and our gas model viewed with an inclination angle of 87° . Gas with a density lower than $0.1 M_\odot \text{pc}^{-3}$ is not shown. We stretch the images such that the b/p bulges and the inner rings have similar sizes for the three galaxies in the plot.

Another interesting feature in this region is the elliptical gas ring surrounding the bar. This ring may contribute to part of the Molecular Ring (Dame et al. 2001; Roman-Duval et al. 2010), which is the high-density and low v_{LOS} strip within $|l| \lesssim 30^\circ$, and the 3 kpc arms in the (l, v) diagram (see the middle panels of Figure 4). One question raised by Kormendy & Bender (2019) is whether our Milky Way is an SB(r)bc galaxy with a gaseous “inner ring.” The answer is probably yes according to our gas models. Note that the inner ring in our model is composed not only of the 3 kpc arms (e.g., suggested by Sevenster & Kalnajs 2001), but also part of the Norma arm and the bar-spiral interfaces that connect to the outer spirals. We show in Figure 9 that, when inclined at an angle of 87° , the inner ring of our fiducial gas model looks quite similar to those observed Milky Way analogs, such as NGC 4565 and NGC 5746 (Kormendy & Bender 2019).

7.3. The Solar Neighborhood (SNd) and the Local Arm

The Local arm was previously assumed to be a spur instead of a major arm, as the latter explanation is not favored by the density wave theory (Yuan 1969). However, recent observations seem to suggest the Local arm has a spatial extent of at least ~ 6 kpc, and its pitch angle, width, and star formation rate are comparable to those of the major arms (e.g., Xu et al. 2013, 2016). If the Local arm is not a spur, then a theoretical explanation is needed to produce this feature together with the other four major arms.

We present one possible scenario to form the Local arm. In our gas models the Local arm is induced by the spiral arm potential described by Equation (5). Note that we only include a four arm spiral perturbation potential, but the corresponding gas flows form a six arm pattern spontaneously. The development of higher-order spiral features (sometimes dubbed as “branches”) has also been found in previous studies (e.g., Martos et al. 2004; Pettitt et al. 2014; Few et al. 2016). We believe the Local arm in our models is related with Φ_6 , which has a clear variation around the solar radius as can be seen in Figure 2. The inner 4:1 resonance of the spiral is 6.8 kpc

(Figure 1), which may also help to shape the Local arm. We have verified that the Local arm co-rotates with the spiral potential ($\Omega_{\text{sp}} = 23 \text{ km s}^{-1} \text{ kpc}^{-1}$) in our models, and thus the bar is probably not relevant to the formation of the Local arm. The scenario presented here is similar to that in Pettitt et al. (2014), where the authors argued the Local and Outer arms may be branches generated by the spiral potential.

We show in Figure 10 that the Local arm has a clear kinematic pattern in the SNd suggested by our models, despite the fact that the local underlying force distribution in Figure 2 is rather smooth. The left panels of Figure 10 plot the gas surface density overlaid with observed HMSFRs (gray points), similar to Figure 8. We further show the zoom-in plots around the SNd in the bottom panels. The Sun is located just inside the Local arm, which has a pitch angle of $\sim 12^\circ$, similar to the value constrained by HMSFRs (Reid et al. 2019). In the middle and right panels we show maps of the residual velocity along the radial and azimuthal directions (i.e., \tilde{V}_R and \tilde{V}_ϕ), which are obtained by subtracting the circular rotation velocity (Figure 1) from the gas velocity fields. The central quadrupole feature in the upper middle panel is evidently due to the bar, and each spiral has its kinematic signature (e.g., \tilde{V} switches sign across spirals) in the residual velocity maps. Due to the presence of the Local arm, the gas in our model is moving outwards and is faster than the circular speed just inside the solar radius, with a typical amplitude of $10\text{--}20 \text{ km s}^{-1}$. This value is comparable to the gas velocities perturbed by the major spiral arms, which are explicitly included in the underlying potential. The observed HMSFRs around the SNd (colored dots) are located mainly outside the solar circle, and they have negative $\tilde{V}_\phi \sim -10 \text{ km s}^{-1}$ (Xu et al. 2013). This seems to agree with the model prediction, but the \tilde{V}_R pattern of the HMSFRs is not quite clear, probably due to the limited number of sources inside the solar circle where the outflow signal is strong.

Interestingly, a stellar \tilde{V}_R pattern similar to that in Figure 10 has been reported by Eilers et al. (2020), and they interpreted it as a dynamical effect of the stellar Local arm. The major differences between Eilers et al. (2020) and this work is we do

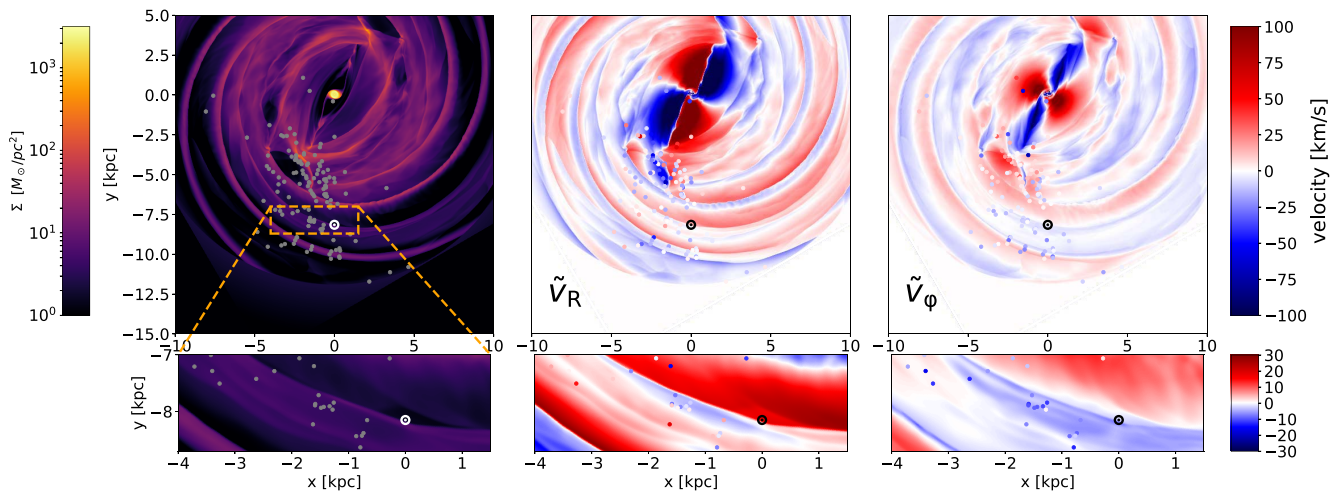


Figure 10. Kinematic maps of the fiducial model with $\Omega_b = 37.5 \text{ km s}^{-1} \text{ kpc}^{-1}$. Left panels: gas surface density overlaid with the locations of HMSFRs (gray dots). The Sun is shown by the solar symbol. Middle panels: Galactocentric residual radial velocity \tilde{V}_R in the model averaged in the z direction. The dots represent the locations of HMSFRs with colors indicating the observed peculiar velocities in the R direction. Right panels: similar to the middle panels, but for Galactocentric residual azimuthal velocity \tilde{V}_ϕ . The residual velocity maps are obtained by subtracting the circular rotation velocity from the gas velocity field at $t = 440 \text{ Myr}$. The bottom panels are the zoom-in views around the SNd defined by the orange dashed box in the upper left panel.

not impose a local spiral potential, but the gaseous Local arm and its related kinematics in our model are spontaneously induced by the four armed pattern of the major stellar spiral arms.

It is still unclear whether the Local arm has an old stellar counterpart. Recent work by Miyachi et al. (2019) found a marginal overdensity of stars near the HMSFR-defined Local arm, with a slightly larger pitch angle. The locations of the young stars in Gaia eDR3 also display an arm feature near the Sun (Poggio et al. 2021; Xu et al. 2021). It is possible that these young stars are formed from the gas arm. Future Galactic surveys may provide a definitive answer on whether there is a massive stellar Local arm composed of old stars near the SNd or not.

8. Discussion

8.1. Moving Groups in the Solar Neighborhood

The gas kinematics prefer $\Omega_b = 37.5\text{--}40 \text{ km s}^{-1} \text{ kpc}^{-1}$ as suggested by our models. It is therefore straightforward to compare this value with other independent measurements. The moving groups in the SNd, especially the Hercules stream, have been extensively used to constrain the bar pattern speed for decades. Dehnen (2000) and Antoja et al. (2014) suggested the Hercules stream is an Outer Lindblad Resonance (OLR) signature of the bar if Ω_b is larger than $\sim 50 \text{ km s}^{-1} \text{ kpc}^{-1}$. The stream could also be reproduced with a bar pattern speed of $\sim 40 \text{ km s}^{-1} \text{ kpc}^{-1}$ by the orbits near the R_{CR} of the bar (e.g., Pérez-Villegas et al. 2017; Monari et al. 2019; Binney 2020; Chiba & Schönrich 2021), and/or the 4:1 resonance of the bar (Hunt & Bovy 2018). We have verified that our Galactic potential in the fiducial models with $\Omega_b = 37.5\text{--}40 \text{ km s}^{-1} \text{ kpc}^{-1}$ also favors a CR-origin explanation, suggesting $\Omega_b = 1.24\text{--}1.32 \Omega_0$ ($\Omega_0 \equiv v_0/R_0$), consistent with $\Omega_b = 1.27 \Omega_0$ obtained by Trick et al. (2021). Note that the Hercules stream may be a bimodal or even trimodal structure as revealed in Gaia DR2 results (Gaia Collaboration et al. 2018; Trick et al. 2019; Asano et al. 2020). Only one of the branches shows a clear phase space snail structure in the $z\text{--}V_z$ plane (Li & Shen 2020). The model that includes the bar resonances alone is probably not enough to split the Hercules

stream into multiple components with different vertical kinematics, hinting at a more complicated formation mechanism.

8.2. Comparing the MW Rotation Curve with Cosmological Simulations

Cosmological simulations offer important insights for understanding the formation and mass assembly history of the Milky Way. For example, the Auriga project (Grand et al. 2017) and the LATTE suite (Wetzel et al. 2016) have provided a number of simulated Milky Way analogs with diverse formation histories in a fully cosmological context, and the models have been widely used in various aspects of Milky Way studies (e.g., Cautun et al. 2020; Fragkoudi et al. 2020; Sanderson et al. 2020; Grand & White 2021).

Here, we constrained the MW potential and rotation curve by modeling different observational data, and it is interesting to compare it with the rotation curves of these cosmological MW analog models. The dynamical bar models of P17 with which we started our analysis used star counts and stellar kinematics in the bulge for an accurate mass determination in the central 2 kpc, and inferred the rotation curve near the Sun ($R = 6\text{--}8 \text{ kpc}$) from terminal velocities assuming circular orbits. Inside 6 kpc the influence of the Galactic bar cannot be neglected, and therefore their rotation curve between both regions was based on fitting a dark matter mass model, i.e., it had a model-dependent component. In this paper we showed that with relatively small modifications to the P17 rotation curve we can reproduce the gas flow and in particular the terminal velocities from the solar radius all the way into the bulge region. The new rotation curve is therefore based on observational data at all of these radii, and is therefore more secure than that of P17. We reiterate here that the observed high gas LOS velocities ($\sim 250 \text{ km s}^{-1}$ within $|l| \lesssim 10^\circ$) are mostly caused by the noncircular flows along the bar, and do not represent the underlying mass distribution in the central region (e.g., see Binney et al. 1991; Chemin et al. 2015).

In Figure 11 we compare the rotation curve (i.e., the mass distribution) inferred by the current work (black line) with five Auriga models from Fragkoudi et al. (2020; colored solid lines) and three LATTE models from Sanderson et al. (2020; colored

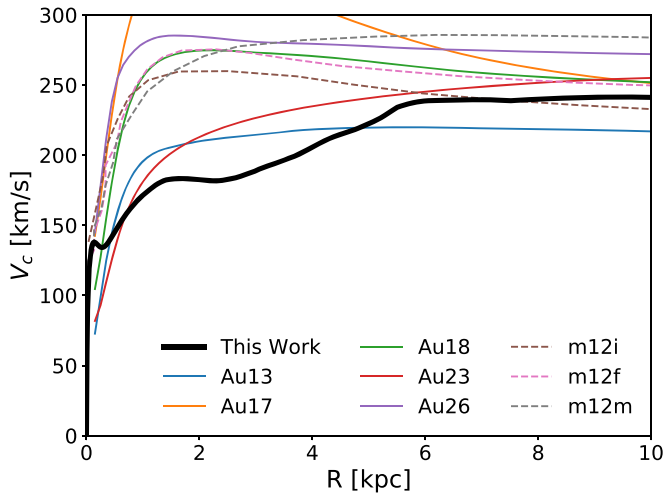


Figure 11. Comparison of the rotation curve from our work (thick black line, same as the solid blue line in Figure 1) and those from the Auriga (solid color lines) and LATTE simulations (dashed color lines).

dashed lines). The five Auriga models are strongly barred galaxies with b/p bulges while the bars in the three LATTE galaxies are weaker and younger (Debattista et al. 2019). Although the two suite zoom-in simulations are different in many aspects (e.g., initial conditions, the merger/mass assembly history, detailed modeling of subgrid physics, numerical resolution, etc.), the rotation curves of the MW analogs in these simulations are all relatively high ($\geq 200 \text{ km s}^{-1}$) in the central $R \lesssim 2 \text{ kpc}$, due to the contribution of a compact bulge. This peak is clearer with a higher numerical resolution, probably caused by the nonlinear star formation history that is sensitive to the resolution and the subgrid physics modules implemented (see the discussion in Grand et al. 2017).

Despite these uncertainties, the combined stellar and gas dynamical models for the MW suggest that in the inner 2 kpc of the Milky Way the mass distribution is less concentrated. The dynamical mass in the bulge volume (i.e., $\lesssim 2 \text{ kpc}$) estimated by P17 is $1.85 \pm 0.05 \times 10^{10} M_{\odot}$, and this already results in a more gently rising rotation curve reaching $\sim 180 \text{ km s}^{-1}$ at $R \sim 2 \text{ kpc}$. But also at larger radii (e.g., $\sim 5 \text{ kpc}$) the inferred rise in the MW rotation curve is slower. Such a rotation curve seems less common in the cosmological simulations, and an interesting question is therefore under what conditions disk galaxies are formed with a slowly rising rotation curve (or a less compact central region). The answer would provide us with more clues to a better understanding of the MW’s formation history.

8.3. Future Improvements

Our current gas models carefully compute the flow of an ideal, isothermal gas in a set of fixed MW potential models. However, we neglect more complicated physical processes such as radiative cooling, star formation, and stellar feedback that may affect many properties of the gas flows. We restrict ourselves to isothermal gas because we would like to understand first how gas with a typical velocity dispersion of $\sim 10 \text{ km s}^{-1}$ evolves in a MW-like potential, which highlights the effects of gravity instead of local gas physics. A clear improvement is therefore to incorporate additional physics in the current fiducial models, similar to other recent attempts to

study the gas structures in the MW (e.g., Baba & Kawata 2020; Pettitt et al. 2020; Reissl et al. 2020).

Another improvement is to use a more accurate potential. We see in Section 6 that the P17 potentials may underestimate the stellar disk and/or the dark matter contributions inside $R \sim 5 \text{ kpc}$, which motivates us to include Φ_{pl} to better match the terminal velocities. The mass distribution outside the solar circle is not well constrained by the current gas models either. In addition, our models assume a fixed potential that neglects the possible perturbations of satellite galaxies (e.g., Antoja et al. 2018; Bland-Hawthorn et al. 2019; Li & Shen 2020). These effects on the gas dynamics in the MW may need to be better investigated in future studies.

9. Summary

We use gas dynamical models to study the gravitational potential and the bar pattern speed of the Milky Way. The base Galactic potentials are from the stellar dynamical models in P17, which are well constrained by the star counts and stellar kinematics. Our gas models provide independent and additional constraints compared to the stellar models, and further improve our understanding of the Galaxy. The main findings in this work are summarized as follows:

- (1) Our model favors a bar pattern speed in the range of $37.5\text{--}40 \text{ km s}^{-1} \text{ kpc}^{-1}$ ($R_{\text{CR}} = 6.0\text{--}6.4 \text{ kpc}$) based on the diagnostics of the observed 3 kpc arms and the forbidden velocity region.
- (2) Our barred potential with a nuclear stellar disk of $6.9 \times 10^8 M_{\odot}$ from Jeans modeling results can generate a central gas disk with a similar size and kinematics compared to the observed CMZ.
- (3) A localized bar-spiral interface with a mass of $0.44 \times 10^8 M_{\odot}$ may be helpful to reproduce the observed large peculiar motions of HMSFRs around the bar end. It also helps to create a gaseous “inner ring” that is similar to external MW analogs.
- (4) The Local arm may be a “branch” that is induced by the four arm spiral potential, as has been suggested by previous studies. In addition, we show this can result in clear gas kinematic patterns around the SNd that agree well with observational data.
- (5) Our fiducial models can generate a steady gas flow pattern that reproduces most of the observed (l , v) features, the terminal velocities, and the peculiar motions of HMSFRs. The rotation curve of the fiducial models has a gently rising shape within $R \sim 5 \text{ kpc}$ instead of a clear peak feature in the central region. The observed high gas LOS velocities ($\sim 250 \text{ km s}^{-1}$ within $|l| \lesssim 10^{\circ}$) are mostly caused by the noncircular flows along the bar, which cannot be used to trace the real mass distribution.

We thank the anonymous referee for suggestions that helped to improve the presentation of the paper. Z.L. would like to thank Robert Grand for sharing the Auriga rotation curves, Jonathan Henshaw for sharing the NH_3 data, and Xiangcheng Ma for helpful discussions. The research presented here is partially supported by the National Key R&D Program of China under grant No. 2018YFA0404501; by the National Natural Science Foundation of China under grant Nos. 12025302, 11773052, and 11761131016; by the “111” Project of the Ministry of Education of China under grant No. B20019;

and by the Chinese Space Station Telescope project. J.S. acknowledges the support of a Newton Advanced Fellowship awarded by the Royal Society and the Newton Fund. O.G. acknowledges the support by Deutsche Forschungsgemeinschaft under grant GZ GE 567/5-1. This work made use of the Gravity Supercomputer at the Department of Astronomy, Shanghai Jiao Tong University, and the facilities of the Center for High Performance Computing at Shanghai Astronomical Observatory.

Software: Athena++ (Stone et al. 2020), Astropy (Astropy Collaboration et al. 2013, 2018), NumPy (Harris et al. 2020), SciPy

(Virtanen et al. 2020), Matplotlib (Hunter 2007), Jupyter Notebook (Kluyver et al. 2016) similaritymeasures (Jekel et al. 2019).

Appendix Different Models

We present the results of different gas models in the Appendix. Figure A1 shows the effects of different bar-spiral interfaces. Figures A2 and A3 shows the effects of different gas effective sound speeds.

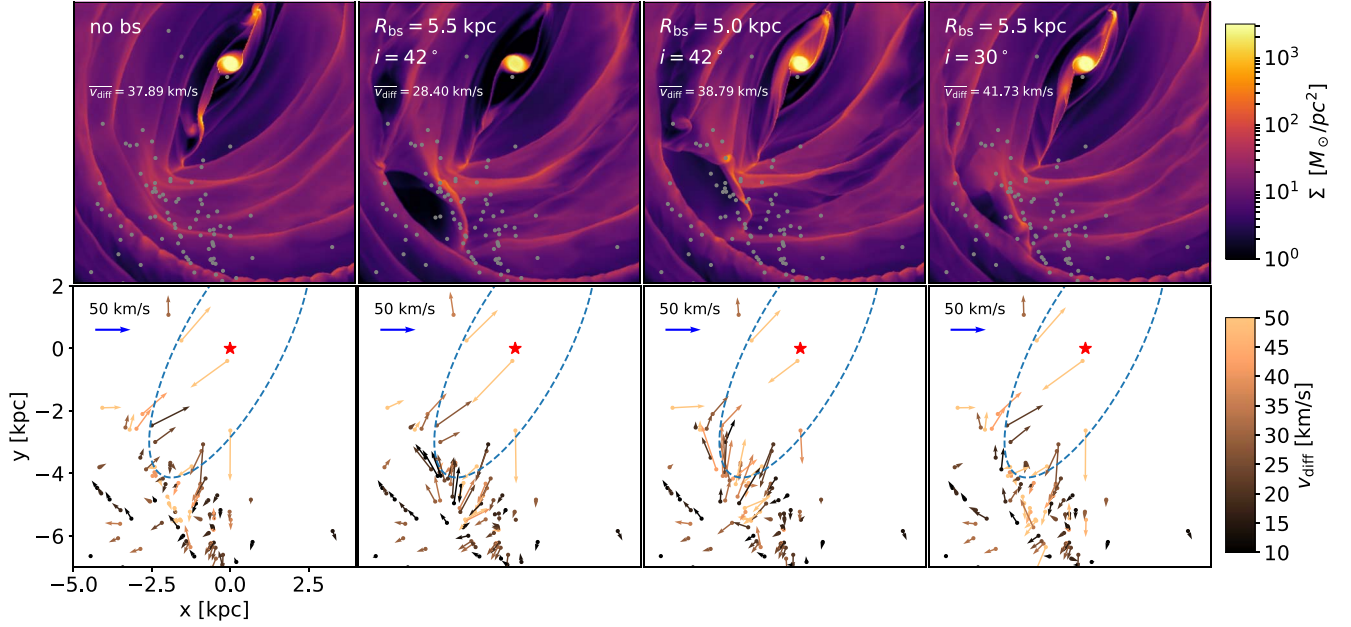


Figure A1. The effects of the bar-spiral interface with different parameters. From left to right: the model without a bar-spiral interface; the model with the bar-spiral interface described in Section 2.4 (i.e., the fiducial model); the model with a bar-spiral interface but adopting a different location of $R_{bs} = 5.0$ kpc; the model with a bar-spiral interface but adopting a different pitch angle of $i = 30^\circ$. Lines and points are the same as in Figure 8. Velocity \bar{v}_{diff} is the average of v_{diff} for the 26 masers within the white dashed box in Figure 8.

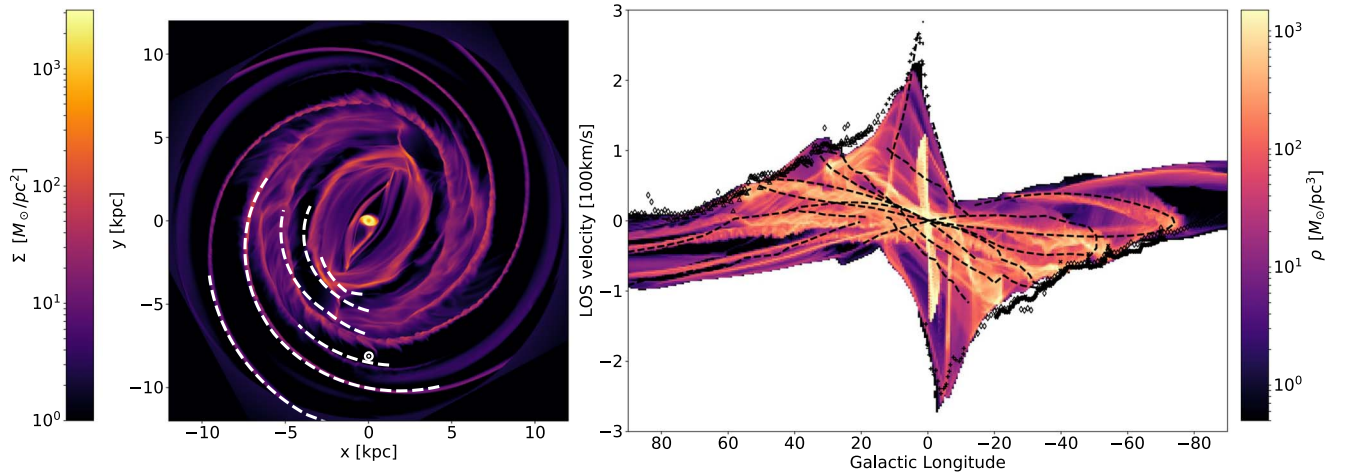


Figure A2. Gas model using the same potential and bar pattern speed as in Figure 5, but with an effective sound speed of 5 km s^{-1} .

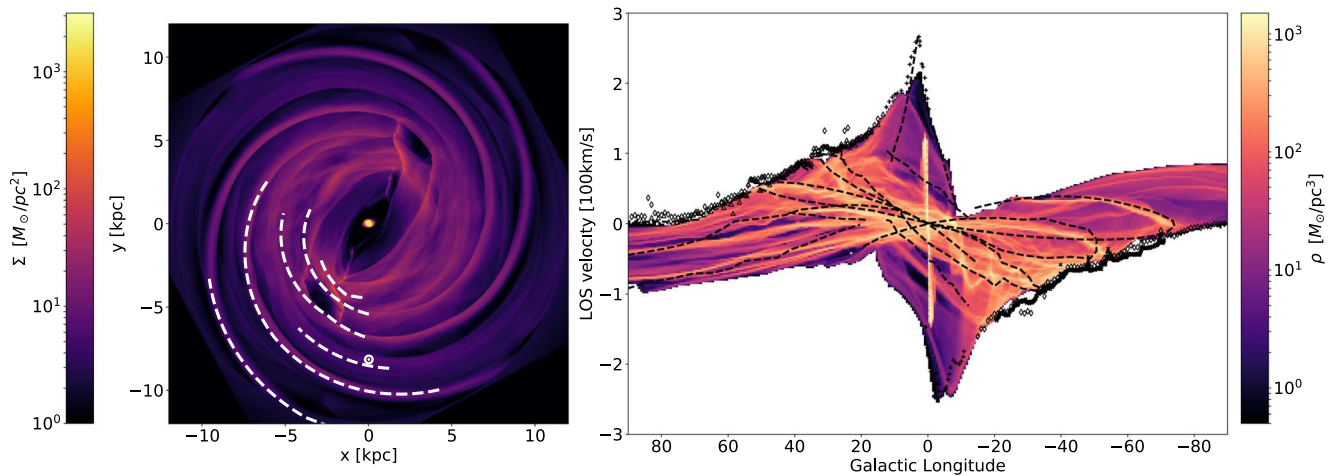


Figure A3. Gas model using the same potential and bar pattern speed as in Figure 5, but with an effective sound speed of 15 km s^{-1} .

ORCID iDs

Zhi Li <https://orcid.org/0000-0002-0627-8009>
 Juntai Shen <https://orcid.org/0000-0001-5604-1643>
 Ortwin Gerhard <https://orcid.org/0000-0003-3333-0033>
 Jonathan P. Clarke <https://orcid.org/0000-0002-2243-178X>

References

- Antoja, T., Helmi, A., Dehnen, W., et al. 2014, *A&A*, **563**, A60
 Antoja, T., Helmi, A., Romero-Gómez, M., et al. 2018, *Natur*, **561**, 360
 Armillotta, L., Krumholz, M. R., Di Teodoro, E. M., & McClure-Griffiths, N. M. 2019, *MNRAS*, **490**, 4401
 Asano, T., Fujii, M. S., Baba, J., et al. 2020, *MNRAS*, **499**, 2416
 Astropy Collaboration, Robitaille, T. P., Tollerud, E. J., et al. 2013, *A&A*, **558**, A33
 Astropy Collaboration, Price-Whelan, A. M., Sipőcz, B. M., et al. 2018, *AJ*, **156**, 123
 Athanassoula, E. 1992, *MNRAS*, **259**, 345
 Baba, J., Asaki, Y., Makino, J., et al. 2009, *ApJ*, **706**, 471
 Baba, J., & Kawata, D. 2020, *MNRAS*, **492**, 4500
 Baba, J., Kawata, D., Matsunaga, N., Grand, R. J. J., & Hunt, J. A. S. 2018, *ApJL*, **853**, L23
 Baba, J., Saitoh, T. R., & Wada, K. 2010, *PASJ*, **62**, 1413
 Bally, J., Stark, A. A., Wilson, R. W., & Henkel, C. 1987, *ApJS*, **65**, 13
 Benjamin, R. A., Churchwell, E., Babler, B. L., Indebetouw, R., et al. 2005, *ApJL*, **630**, L149
 Binney, J. 2020, *MNRAS*, **495**, 895
 Binney, J., Gerhard, O. E., Stark, A. A., Bally, J., & Uchida, K. I. 1991, *MNRAS*, **252**, 210
 Bissantz, N., Englmaier, P., & Gerhard, O. 2003, *MNRAS*, **340**, 949
 Bland-Hawthorn, J., & Gerhard, O. 2016, *ARA&A*, **54**, 529
 Bland-Hawthorn, J., Sharma, S., Tepper-García, T., et al. 2019, *MNRAS*, **486**, 1167
 Bovy, J., & Rix, H.-W. 2013, *ApJ*, **779**, 115
 Brunthaler, A., Reid, M. J., Menten, K. M., et al. 2011, *AN*, **332**, 461
 Burton, W. B. 1976, *ARA&A*, **14**, 275
 Burton, W. B., & Liszt, H. S. 1978, *ApJ*, **225**, 815
 Burton, W. B., & Liszt, H. S. 1993, *A&A*, **274**, 765
 Cabrera-Lavers, A., González-Fernández, C., Garzón, F., Hammersley, P. L., & López-Corredoira, M. 2008, *A&A*, **491**, 781
 Cautun, M., Benítez-Llambay, A., Deason, A. J., et al. 2020, *MNRAS*, **494**, 4291
 Chatzopoulos, S., Fritz, T. K., Gerhard, O., et al. 2015, *MNRAS*, **447**, 948
 Chemin, L., Renaud, F., & Soubiran, C. 2015, *A&A*, **578**, A14
 Chiba, R., Friske, J. K. S., & Schönrich, R. 2021, *MNRAS*, **500**, 4710
 Chiba, R., & Schönrich, R. 2021, *MNRAS*, **505**, 2412
 Clarke, J. P., Wegg, C., Gerhard, O., et al. 2019, *MNRAS*, **489**, 3519
 Clemens, D. P. 1985, *ApJ*, **295**, 422
 Combes, F. 1996, ASP Conf. Ser. 91, IAU Coll. 157: Barred Galaxies, ed. R. Buta, D. A. Crocker, & B. G. Elmegreen, (San Francisco, CA: ASP), 286
 Combes, F., & Sanders, R. H. 1981, *A&A*, **96**, 164
 Comerón, S., Knapen, J. H., Beckman, J. E., et al. 2010, *MNRAS*, **402**, 2462
 Dame, T. M., Hartmann, D., & Thaddeus, P. 2001, *ApJ*, **547**, 792
 Dame, T. M., & Thaddeus, P. 2011, *ApJL*, **734**, L24
 de Vaucouleurs, G. 1959, *HDP*, **53**, 275
 Debattista, V. P., Gonzalez, O. A., Sanderson, R. E., et al. 2019, *MNRAS*, **485**, 5073
 Dehnen, W. 2000, *AJ*, **119**, 800
 Dwek, E., Arendt, R. G., Hauser, M. G., et al. 1995, *ApJ*, **445**, 716
 Eilers, A.-C., Hogg, D. W., Rix, H.-W., et al. 2020, *ApJ*, **900**, 186
 Eilers, A.-C., Hogg, D. W., Rix, H.-W., & Ness, M. K. 2019, *ApJ*, **871**, 120
 Englmaier, P., & Gerhard, O. 1997, *MNRAS*, **287**, 57
 Englmaier, P., & Gerhard, O. 1999, *MNRAS*, **304**, 512
 Few, C. G., Dobbs, C., Pettitt, A., & Konstantin, L. 2016, *MNRAS*, **460**, 4382
 Fich, M., Blitz, L., & Stark, A. A. 1989, *ApJ*, **342**, 272
 Fragkoudi, F., Athanassoula, E., & Bosma, A. 2016, *MNRAS*, **462**, L41
 Fragkoudi, F., Grand, R. J. J., Pakmor, R., et al. 2020, *MNRAS*, **494**, 5936
 Fux, R. 1999, *A&A*, **345**, 787
 Gaia Collaboration, Katz, D., Antoja, T., et al. 2018, *A&A*, **616**, A11
 Gallego-Cano, E., Schödel, R., Nogueras-Lara, F., et al. 2020, *A&A*, **634**, A71
 Georgelin, Y. M., & Georgelin, Y. P. 1976, *A&A*, **49**, 57
 Gerhard, O. E., & Vietri, M. 1986, *MNRAS*, **223**, 377
 Glover, S. C. O., & Clark, P. C. 2012, *MNRAS*, **421**, 9
 Gouda, N. 2012, ASP Conf. Ser. 458, Galactic Archaeology: Near-Field Cosmology and the Formation of the Milky Way, ed. W. Aoki et al. (San Francisco, CA: ASP), 417
 Grand, R. J. J., Gómez, F. A., Marinacci, F., et al. 2017, *MNRAS*, **467**, 179
 Grand, R. J. J., & White, S. D. M. 2021, *MNRAS*, **501**, 3558
 Gravity Collaboration, Abuter, R., Amorim, A., et al. 2019, *A&A*, **625**, L10
 Hammersley, P. L., Garzón, F., Mahoney, T. J., López-Corredoira, M., & Torres, M. A. P. 2000, *MNRAS*, **317**, L45
 Harris, C. R., Millman, K. J., van der Walt, S. J., et al. 2020, *Natur*, **585**, 357
 Hatchfield, H. P., Battersby, C., Keto, E., et al. 2020, *ApJS*, **251**, 14
 Hatchfield, H. P., Sormani, M. C., Tress, R. G., et al. 2021, *ApJ*, **922**, 79
 Henshaw, J. D., Longmore, S. N., Kruijssen, J. M. D., et al. 2016, *MNRAS*, **457**, 2675
 Hilmi, T., Minchev, I., Buck, T., et al. 2020, *MNRAS*, **497**, 933
 Hobbs, D., Brown, A., Høg, E., et al. 2019, arXiv:1907.12535
 Hou, L. G., & Han, J. L. 2014, *A&A*, **569**, A125
 Hunt, J. A. S., & Bovy, J. 2018, *MNRAS*, **477**, 3945
 Hunter, J. D. 2007, *CSE*, **9**, 90
 Jekel, C. F., Venter, G., Venter, M. P., Stander, N., & Haftka, R. T. 2019, *Int. J. Mater. Form.*, **12**, 355
 Junqueira, T. C., Chiappini, C., Lépine, J. R. D., Minchev, I., & Santiago, B. X. 2015, *MNRAS*, **449**, 2336
 Junqueira, T. C., Lépine, J. R. D., Braga, C. A. S., & Barros, D. A. 2013, *A&A*, **550**, A91
 Kim, S. S., Saitoh, T. R., Jeon, M., et al. 2011, *ApJL*, **735**, L11
 Kim, W.-T., & Ostriker, E. C. 2006, *ApJ*, **646**, 213
 Kim, W.-T., Seo, W.-Y., Stone, J. M., Yoon, D., & Teuben, P. J. 2012, *ApJ*, **747**, 60

- Kluyver, T., Ragan-Kelley, B., Pérez, F., et al. 2016, in *Positioning and Power in Academic Publishing: Players, Agents and Agendas*, ed. F. Loizides & B. Schmidt (Amsterdam: IOS Press), 87
- Kormendy, J., & Bender, R. 2019, *ApJ*, **872**, 106
- Langer, W. D., Velusamy, T., Morris, M. R., Goldsmith, P. F., & Pineda, J. L. 2017, *A&A*, **599**, A136
- Laporte, C. F. P., Minchev, I., Johnston, K. V., & Gómez, F. A. 2019, *MNRAS*, **485**, 3134
- Launhardt, R., Zylka, R., & Mezger, P. G. 2002, *A&A*, **384**, 112
- Li, Z., Gerhard, O., Shen, J., Portail, M., & Wegg, C. 2016, *ApJ*, **824**, 13
- Li, Z., Shen, J., & Kim, W.-T. 2015, *ApJ*, **806**, 150
- Li, Z., Shen, J., & Schive, H.-Y. 2020, *ApJ*, **889**, 88
- Li, Z.-Y., & Shen, J. 2015, *ApJL*, **815**, L20
- Li, Z.-Y., & Shen, J. 2020, *ApJ*, **890**, 85
- Liszt, H. S., & Burton, W. B. 1980, *ApJ*, **236**, 779
- Longmore, S. N., Walsh, A. J., Purcell, C. R., et al. 2017, *MNRAS*, **470**, 1462
- Mangilli, A., Aumont, J., Bernard, J. P., et al. 2019, *A&A*, **630**, A74
- Martinez-Valpuesta, I., Shlosman, I., & Heller, C. 2006, *ApJ*, **637**, 214
- Martos, M., Hernandez, X., Yáñez, M., Moreno, E., & Pichardo, B. 2004, *MNRAS*, **350**, L47
- McClure-Griffiths, N. M., & Dickey, J. M. 2007, *ApJ*, **671**, 427
- McGaugh, S. S. 2019, *ApJ*, **885**, 87
- Minchev, I., Famaey, B., Quillen, A. C., et al. 2012, *A&A*, **548**, A126
- Miyachi, Y., Sakai, N., Kawata, D., et al. 2019, *ApJ*, **882**, 48
- Molinari, S., Bally, J., Noriega-Crespo, A., et al. 2011, *ApJL*, **735**, L33
- Monari, G., Famaey, B., Siebert, A., Wegg, C., & Gerhard, O. 2019, *A&A*, **626**, A41
- Ness, M., & Lang, D. 2016, *AJ*, **152**, 14
- Nishiyama, S., Yasui, K., Nagata, T., et al. 2013, *ApJL*, **769**, L28
- Nogueras-Lara, F., Schödel, R., Gallego-Calvente, A. T., et al. 2019, *NatAs*, **4**, 377
- Pérez-Villegas, A., Portail, M., Wegg, C., & Gerhard, O. 2017, *ApJL*, **840**, L2
- Pettitt, A. R., Dobbs, C. L., Acreman, D. M., & Bate, M. R. 2015, *MNRAS*, **449**, 3911
- Pettitt, A. R., Dobbs, C. L., Acreman, D. M., & Price, D. J. 2014, *MNRAS*, **444**, 919
- Pettitt, A. R., Ragan, S. E., & Smith, M. C. 2020, *MNRAS*, **491**, 2162
- Poggio, E., Drimmel, R., Cantat-Gaudin, T., et al. 2021, *A&A*, **651**, A104
- Portail, M., Gerhard, O., Wegg, C., & Ness, M. 2017, *MNRAS*, **465**, 1621
- Quillen, A. C., Dougherty, J., Bagley, M. B., Minchev, I., & Comparella, J. 2011, *MNRAS*, **417**, 762
- Raha, N., Sellwood, J. A., James, R. A., & Kahn, F. D. 1991, *Natur*, **352**, 411
- Regan, M. W., & Teuben, P. J. 2004, *ApJ*, **600**, 595
- Reid, M. J., Dame, T. M., Menten, K. M., & Brunthaler, A. 2016, *ApJ*, **823**, 77
- Reid, M. J., Menten, K. M., Brunthaler, A., et al. 2014, *ApJ*, **783**, 130
- Reid, M. J., Menten, K. M., Brunthaler, A., et al. 2019, *ApJ*, **885**, 131
- Reissl, S., Stil, J. M., Chen, E., et al. 2020, *A&A*, **642**, A201
- Ridley, M. G. L., Sormani, M. C., Treß, R. G., Magorrian, J., & Klessen, R. S. 2017, *MNRAS*, **469**, 2251
- Roberts Jr., W. W., Huntley, J. M., & van Albada, G. D. 1979, *ApJ*, **233**, 67
- Rodriguez-Fernandez, N. J., & Combes, F. 2008, *A&A*, **489**, 115
- Roe, P. L. 1981, *JCoPh*, **43**, 357
- Roman-Duval, J., Jackson, J. M., Heyer, M., Rathborne, J., & Simon, R. 2010, *ApJ*, **723**, 492
- Russeil, D. 2003, *A&A*, **397**, 133
- Salas, J. M., Naoz, S., & Morris, M. R. 2020, arXiv:2010.04170
- Sandage, A. 1961, *The Hubble Atlas of Galaxies* (Washington, DC: Carnegie Institution)
- Sanders, J. L., Smith, L., & Evans, N. W. 2019, *MNRAS*, **488**, 4552
- Sanderson, R. E., Wetzel, A., Loebman, S., et al. 2020, *ApJS*, **246**, 6
- Schönrich, R., Aumer, M., & Sale, S. E. 2015, *ApJL*, **812**, L21
- Schönrich, R., Binney, J., & Dehnen, W. 2010, *MNRAS*, **403**, 1829
- Sellwood, J. A., Trick, W. H., Carlberg, R. G., Coronado, J., & Rix, H.-W. 2019, *MNRAS*, **484**, 3154
- Seo, W.-Y., & Kim, W.-T. 2014, *ApJ*, **792**, 47
- Seo, W.-Y., Kim, W.-T., Kwak, S., et al. 2019, *ApJ*, **872**, 5
- Sevenster, M. N., & Kalnajs, A. J. 2001, *AJ*, **122**, 885
- Shen, J., Rich, R. M., Kormendy, J., et al. 2010, *ApJL*, **720**, L72
- Shen, J., & Zheng, X.-W. 2020, *RAA*, **20**, 159
- Simion, I. T., Belokurov, V., Irwin, M., et al. 2017, *MNRAS*, **471**, 4323
- Sofue, Y., Honma, M., & Omodaka, T. 2009, *PASJ*, **61**, 227
- Sormani, M. C., & Barnes, A. T. 2019, *MNRAS*, **484**, 1213
- Sormani, M. C., Binney, J., & Magorrian, J. 2015a, *MNRAS*, **449**, 2421
- Sormani, M. C., Binney, J., & Magorrian, J. 2015b, *MNRAS*, **451**, 3437
- Sormani, M. C., Binney, J., & Magorrian, J. 2015c, *MNRAS*, **454**, 1818
- Sormani, M. C., Magorrian, J., Nogueras-Lara, F., et al. 2020a, *MNRAS*, **499**, 7
- Sormani, M. C., Treß, R. G., Glover, S. C. O., et al. 2019, *MNRAS*, **488**, 4663
- Sormani, M. C., Tress, R. G., Glover, S. C. O., et al. 2020b, *MNRAS*, **497**, 5024
- Sormani, M. C., Treß, R. G., Ridley, M., et al. 2018, *MNRAS*, **475**, 2383
- Stone, J. M., Tomida, K., White, C., & Felker, K. G. 2019, *Athena++: Radiation GR magnetohydrodynamics code*, Astrophysics Source Code Library, <http://ascl.net/1912.005>
- Stone, J. M., Tomida, K., White, C. J., & Felker, K. G. 2020, *ApJS*, **249**, 4
- Tamburro, D., Rix, H. W., Leroy, A. K., et al. 2009, *AJ*, **137**, 4424
- Tress, R. G., Sormani, M. C., Glover, S. C. O., et al. 2020, *MNRAS*, **499**, 4455
- Trick, W. H., Coronado, J., & Rix, H.-W. 2019, *MNRAS*, **484**, 3291
- Trick, W. H., Fragkoudi, F., Hunt, J. A. S., Mackereth, J. T., & White, S. D. M. 2021, *MNRAS*, **500**, 2645
- VERA Collaboration, Hirota, T., Nagayama, T., et al. 2020, *PASJ*, **72**, 50
- Virtanen, P., Gommers, R., Oliphant, T. E., et al. 2020, *NatMe*, **17**, 261
- Wada, K., & Koda, J. 2004, *MNRAS*, **349**, 270
- Walter, F., Brinks, E., de Blok, W. J. G., et al. 2008, *AJ*, **136**, 2563
- Wegg, C., & Gerhard, O. 2013, *MNRAS*, **435**, 1874
- Wegg, C., Gerhard, O., & Portail, M. 2015, *MNRAS*, **450**, 4050
- Wetzel, A. R., Hopkins, P. F., Kim, J.-H., et al. 2016, *ApJL*, **827**, L23
- White, C. J., Stone, J. M., & Gammie, C. F. 2016, *ApJS*, **225**, 22
- Xu, Y., Hou, L. G., Bian, S. B., et al. 2021, *A&A*, **645**, L8
- Xu, Y., Hou, L.-G., & Wu, Y.-W. 2018, *RAA*, **18**, 146
- Xu, Y., Li, J. J., Reid, M. J., et al. 2013, *ApJ*, **769**, 15
- Xu, Y., Reid, M., Dame, T., et al. 2016, *SciA*, **2**, e1600878
- Yuan, C. 1969, *ApJ*, **158**, 871